Mon. Not. R. Astron. Soc. **000**, 1–18 (2004) Printed 5 February 2008 (MN LaTeX style file v2.2)

arXiv:astro-ph/0507095v1 5 Jul 2005

Radial and 2D Colour Properties of E+A Galaxies

Chisato Yamauchi[1,2]* and Tomotsugu Goto[3]†
[1]Department of Physics and Astrophysics, Nagoya University, Chikusa-ku, Nagoya 464-8602, Japan
[2]National Astronomical Observatory, 2-21-1 Osawa, Mitaka, Tokyo 181-8588, Japan
[3]Department of Physics and Astronomy, The Johns Hopkins University, 3400 North Charles Street, Baltimore, MD 21218-2686, USA

5 February 2008

ABSTRACT

We investigate the radial colour gradient and two-dimensional (2D) colour properties of 22 E+A galaxies with $5.5\text{Å} <$ Hδ EW $< 8.5\text{Å}$ and 49 normal early-type galaxies as a control sample at a redshift of < 0.2 in the Second Data Release of the Sloan Digital Sky Survey. We found that a substantial number of E+A galaxies exhibit positive slopes of radial colour gradient (bluer gradients toward the centre) which are seldom seen in normal early-type galaxies. We found irregular 'Colour Morphologies' – asymmetrical and clumpy patterns – at the centre of $g-r$ and $r-i$ 2D colourmaps of E+A galaxies with positive slopes of colour gradient. Kolomogorov-Smirnov two-sample tests show that $g-r$ and $r-i$ colour gradient distributions of E+A galaxies differ from those of early-type galaxies with a more than 99.99% significance level. We also found a tight correlation between radial colour gradients and colours, and between radial colour gradients and 4000Å break in the E+A sample; E+A galaxies which exhibit bluer colour or weaker D_{4000} tend to have positive slopes of radial colour gradient. We compared the GISSEL model and E+A's observational quantities, Hδ EW, D_{4000} and $u-g$ colour, and found that almost all our E+A galaxies are situated along a single evolution track. Therefore, these results are interpreted as E+A galaxies evolving from Hδ EW $\sim 8\text{Å}$ to Hδ EW $\sim 5\text{Å}$, with colour gradients changing from positive to negative, and with the irregular 2D colourmap becoming smoother, during a time scale of ∼300 Myr. Our results favor the hypothesis that E+A galaxies are post-starburst galaxies caused by merger/interaction, having undergone a centralized violent starburst.

Key words: galaxies: general

1 INTRODUCTION

Dressler & Gunn (1983, 1992) discovered galaxies with mysterious spectra while investigating high redshift cluster galaxies. These galaxies had strong Balmer absorption lines with no emission in [OII]. They were named "E+A" galaxies, since their spectra resembled a superposition of those of elliptical galaxies (Mg$_{5175}$, Fe$_{5270}$ and Ca$_{3934,3468}$ absorption lines) and those of A-type stars (Strong Balmer absorption)[1]. Since the lifetime of an A-type star is about 1 Gyr, the existence of strong Balmer absorption lines shows that these galaxies have experienced starburst within the last Gyr. However, they show no sign of on-going star formation as non-detection in the [OII] emission line indicates. Therefore E+A galaxies are interpreted as post-starburst galaxies, that is, galaxies which have undergone truncated starburst (Dressler & Gunn 1983, 1992; Couch & Sharples 1987; MacLaren, Ellis & Couch 1988; Newberry, Boroson & Kirshner 1990; Fabricant, McClintock & Bautz 1991; Abraham et al. 1996).

At first, "E+A" galaxies were found in cluster regions, both in low redshift clusters (Franx 1993; Caldwell et al. 1993; Caldwell & Rose 1997; Castander et al. 2001; Rose et al. 2001) and high redshift clusters (Sharples et al. 1985; Lavery & Henry 1986; Couch & Sharples 1987; Broadhurst, Ellis & Shanks 1988; Fabricant, McClintock & Bautz 1991; Belloni et al. 1995; Barger et al. 1996; Fisher et al. 1998; Morris et al. 1998; Couch et al. 1998; Dressler et al. 1999). Therefore, a cluster specific phenomenon (e.g., Goto et al. 2003b) was thought to be responsible for the violent star formation history of E+A galaxies. A ram-pressure stripping model (Spitzer & Baade 1951; Gunn & Gott 1972; Farouki & Shapiro 1980; Kent 1981; Abadi, Moore & Bower 1999; Fujita & Nagashima 1999; Quilis, Moore & Bower 2000; Fujita 2004; Fujita & Goto 2004) as well as tides from the cluster potential (e.g., Fujita 2004) may first accelerate star formation of cluster galaxies and later turn it off. However, recent large surveys of the nearby universe found many

---

* E-mail:cyamauch@a.phys.nagoya-u.ac.jp
† E-mail:tomo@jhu.edu

[1] Because the spectra of elliptical galaxies are characterized by K stars, these galaxies are sometimes called "K+A" galaxies (e.g., Franx 1993; Dressler et al. 1999; Bartholomew, Rose & Gaba 2001). Following the first discovery, we refer to them as "E+A" throughout this work.

© 2004 RAS

E+A galaxies in the field regions (Goto 2003, 2005; Goto et al. 2003c; Quintero 2004). At the very least, it is clear that these E+A galaxies in the field regions cannot be explained by a physical mechanism that works in the cluster region. E+A galaxies have often been thought to be transitional objects during cluster galaxy evolution, evolving phenomena such as the Butcher-Oemler effect (e.g., Goto et al. 2003a), the morphology-density relation (e.g., Goto et al. 2003e), and the correlation between various properties of the galaxies with the environment (e.g., Tanaka et al. 2004). However, explaining cluster galaxy evolution using E+A galaxies may not be realistic anymore.

One possible explanation for E+A phenomena is dust-enshrouded star formation, where E+A galaxies are actually star-forming, but emission lines are invisible in optical wavelengths due to heavy obscuration by dust. As a variant, Poggianti & Wu (2000) presented the selective dust extinction hypothesis, where dust extinction is dependent on stellar age, since the youngest stars inhabit very dusty star-forming HII regions while older stars have had time to migrate out of such dusty regions. If O, B-type stars in E+A galaxies are embedded in dusty regions and only A-type stars have long enough lifetimes (∼1 Gyr) to move out from such regions, this scenario can naturally explain the E+A phenomena. A straightforward test for these scenarios is to observe in radio wavelengths where the dust obscuration is negligible. At 20cm radio wavelengths, the synchrotron radiation from electrons accelerated by supernovae can be observed. Therefore, in the absence of a radio-loud active nucleus, the radio flux of a star-forming galaxy can be used to estimate its current massive star formation rate (SFR) (Condon 1992; Kennicutt 1998; Hopkins et al. 2003). Smail et al. (1999) performed such a radio observation and found that among 8 galaxies detected in radio, 5 have strong Balmer absorption with no detection in [OII]. They concluded that massive stars are currently forming in these 5 galaxies. Owen et al. (1999) investigated the radio properties of galaxies in a rich cluster at $z \sim 0.25$ (A2125) and found that optical line luminosities (e.g., Hα+[NII]) were often weaker than one would expect for the SFRs implied by the radio emission. Miller & Owen (2001) observed radio continua of 15 E+A galaxies and detected moderate levels of star formation in only 2 of them. Goto (2004) performed 20cm radio continuum observation of 36 E+A galaxies, and none of them are detected in 20cm, suggesting that E+A galaxies are not dusty-starburst galaxies.

Alternatively, galaxy-galaxy interaction has been known to trigger star formation in the pair of galaxies (Schweizer 1982; Lavery & Henry 1988; Liu & Kennicutt 1995a,b; Schweizer 1996; Nikolic, Cullen & Alexander 2004). Oegerle, Hill & Hoessel (1991) found a nearby E+A galaxy with a tidal tail feature. High resolution Hubble Space Telescope imaging supported the galaxy-galaxy interaction scenario by showing some post-starburst (E+A) galaxies in high redshift clusters as having disturbed or interacting signatures (Couch et al. 1994, 1998; Dressler et al. 1994; Oemler, Dressler & Butcher 1997). Liu & Kennicutt (1995a,b) observed 40 merging/interacting systems and found that some of their spectra resemble E+A galaxies. Bekki, Shioya & Couch (2001) modeled galaxy-galaxy mergers with dust extinction, confirming that such systems can produce spectra which evolve into E+A spectra. Recently, Goto et al. (2003d); Goto (2005) found that young E+A galaxies have more companion galaxies within 100 kpc, providing strong support for the merger/interaction origin of E+A galaxies.

As is mentioned above, most of the previous work is focused on the global properties of E+A galaxies. Needless to say, investigation of the internal properties of E+A galaxies such as age and metallicity gradients is also indispensable in solving the E+A mystery. Do E+A galaxies leave traces of merger/interaction? Where do the traces remain, in a centralized or decentralized starburst? The elucidation of these questions is essential in testing E+A evolution scenarios. Norton et al. (2001) performed long-slit spectroscopic observation of 21 E+A galaxies, and found young stellar populations of E+A galaxies are more centrally concentrated than older populations, and old components of E+A galaxies conform to the Faber-Jackson relation. Bartholomew, Rose & Gaba (2001) also reported that E+A galaxies on average tend to have slightly bluer radial gradients toward the centre than do normal early-type galaxies. Yang et al. (2004) presented HST observations of the five bluest E+A galaxies with $z \sim 0.1$ and reported details of disturbed morphologies and detected compact sources associated with E+A which are consistent with the brightest clusters in nearby starburst galaxies. Although these are important results, previous work often lacked statistical significance, since E+A galaxies are extremely rare. In addition, it is important to understand the spatial properties of E+A galaxies along an evolutionary sequence. Furthermore, there is a contamination problem in the E+A sample selected without using Hα. Kennicutt (1992a,b) shows, Hα is the best star formation indicator in the optical wavelength since it is a strong line and it has fewer uncertainties (e.g., dust extinction, self-absorption, metallicity dependence) than the other lines. Indeed, Goto (2003) reported that an E+A sample without Hα cut-off contains ∼50% contamination. Blake et al. (2004) also found that the criterion using Hδ and [OII] leads to a significant sub-population of disk systems with detectable Hα emissions. We stress that a clean sample selection is essential in order to study a rare population of galaxies such as E+As.

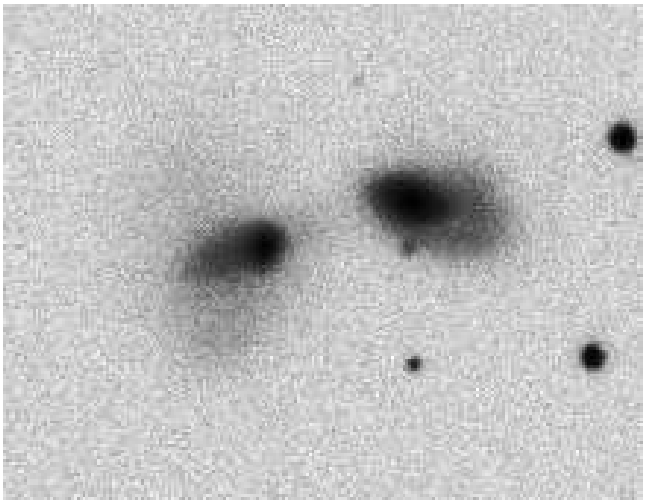

Figure 1. SDSS r-band image of one of the nearest E+A galaxies (left;z=0.034) captured from the SDSS DR2 sample. The image size is 86.3 arcsec × 66.9 arcsec. Note the dramatic tidal tails.

In this paper, we use publicly available *true* E+A galaxies (without Hα nor [OII] emission) selected from the Sloan Digital Sky Survey (SDSS, York et al. 2000; Early Data Release, Stoughton et al. 2002, hereafter EDR; First Data Release, Abazajian et al. 2003, hereafter DR1; Second Data Release, Abazajian et al. 2004, hereafter DR2) by Goto (2005). Both broad-band imaging and the spectroscopic survey of 10,000 deg^2 of SDSS provides us with the first opportunity to study E+A galaxies in a very large number. Goto (2005) analyzed ∼250,000 galaxy spectra in the DR2, and the number of E+A homogeneous galaxies reached 266. The SDSS imaging is somewhat poor (typical seeing size is $\sim$1.5$''$) compared with 8m-class telescopes or HST, but this sample includes very nearby or large E+A galaxies like Figure 1, which exhibits dramatic tidal tails or conspicuous disturbed morphologies. We then select 22 E+A galaxies with $z < 0.2$, large apparent size, and more strict criteria $5.5\text{Å} < H\delta$ EW, $-1.0\text{Å} <$ Hα EW and $-2.5\text{Å} <$ OII EW (a positive sign is absorption), and investigate spatial properties; 2D colourmaps and $g{-}r$ and $r{-}i$ radial colour gradients. The radial colour gradients are compared with spectroscopic properties, and we compare these properties with evolution scenarios using SED models in order to understand the evolutionary sequence of E+A galaxies.

This paper is organized as follows: In section 2, the definitions of two galaxy samples are summarized, as well as the spectroscopic and imaging data. In section 3, we explain the reduction of the imaging data, e.g. an image convolution, position matching between passbands, a review of the concentration index and a definition of radial colour gradients. In section 4, we briefly describe our E+A morphologies, and study 2D $g{-}r$ and $r{-}i$ colour properties, 2D colourmaps and radial colour gradients, with relations to other photometric/spectroscopic properties. We then investigate the evolution scenario for E+A radial colour gradients using a comparison between SED models and our observational data. In section 5, we discuss our results with other E+A-related studies. Our conclusions are presented in section 6. The cosmological parameters adopted throughout this paper are $H_0 = 75\text{kms}^{-1}\text{Mpc}^{-1}$, and $(\Omega_m, \Omega_\Lambda, \Omega_k) = (0.3, 0.7, 0.0)$.

2 DATA SAMPLES

Our E+A galaxies are selected from the publicly available catalog described in Goto (2005). The mother sample of this catalog contains $\sim$250,000 objects classified as galaxies with spectroscopic information in SDSS DR2 (Abazajian et al. 2004). Goto (2005) selected 266 E+A galaxies as those with $5.0\text{Å} <$ Hδ EW, $-3.0\text{Å} <$ Hα EW and $-2.5\text{Å} <$ [OII] EW (absorption lines have a positive sign) after redshift (> 0.01) and S/N ($>$10 per pixel) cut-off.

We have restricted our targets to those galaxies which have a redshift z of less than 0.2 and an apparent size of a_{60} (Petrosian 60% flux semi-major axis; described in section 3) more than 2.82$''$ to maintain enough sampling points for radial colour gradients. This selection leaves 50 E+A galaxies. To minimize contamination of our E+A galaxies with remaining star formation activity, we set more strict spectroscopic criteria $5.5\text{Å} <$ Hδ EW and $-1.0\text{Å} <$ Hα EW, and finally, we are left with 22 E+A galaxies of greater purity.

We also randomly selected 50 normal early-type galaxies within $z < 0.2$ as a control sample from objects classified as galaxies in the SDSS DR2 catalog. The normal early-type galaxies are selected using the elliptical-based concentration index, C_e (Yamauchi et al. 2005), a ratio of Petrosian 50% flux semi-major axis to 90% flux semi-major axis (See section 3); $C_e < 0.33$ for early-type galaxies (Shimasaku et al. 2001). Although the standard (inverse) concentration index $C = r_{50}/r_{90}$ defined with the Petrosian flux in the circular apertures is significantly affected by inclination, the effect of inclination is removed with the use of elliptical apertures (Yamauchi et al. 2005). The cut-off size of a_{60} is the same as that of E+A galaxies. But this subsample contains 1 galaxy with a deblending problem, which we eliminated. Finally, we use 49 normal early-type galaxies as a control sample.

The spectroscopic data, Hδ, Hα and [OII] equivalent width (EWs) and their errors are measured by the flux-summing method described in Goto (2005) (See also Goto et al. 2003c). The values of 4000Å break(D_{4000}) in our paper are the reciprocal numbers of values in the SDSS catalog. We use DR2 atlas images (Stoughton et al. 2002) as imaging data to calculate 2D colourmaps and radial colour gradients of $g{-}r$ and $r{-}i$, and concentration index C_e. The photometric system, imaging hardware and astrometric calibration of SDSS are described in detail elsewhere (Fukugita et al. 1996; Gunn et al. 1998; Hogg et al. 2001; Smith et al. 2002; Pier et al. 2003).

3 DATA REDUCTIONS

From the SDSS database, we can easily download the deblended galaxy images, called ‘atlas images’, by fpAtlas file in which images are archived using Rice compression. In the SDSS images, however, the seeing sizes differ from passband to passband, and the relation between physical and imaging positions of a passband on an Atlas image is not equal to others, but slightly differs. Therefore we cannot directly compose g- and r-band images, or r- and i-band images using the coordinates given by the fpAtlas file. We adjust the positions of the multi-band images in the following way:

First, we smear all images except those with the worst seeing $\sigma_{\max}$ among the passbands to equalize the seeing sizes of all passbands. Assuming that the point-spread function is Gaussian, images are convolved with a Gaussian function of σ_c,

$$\sigma_\mathrm{c} = \sqrt{\sigma_{\max}^2 - \sigma^2}, \tag{1}$$

where σ is the actual seeing of each image derived from the `psf_width` parameter in tsField files:

$$\sigma = (\mathtt{psf\_width}/1.06)/2.35, \tag{2}$$

where `psf_width` is equivalent to 1.06 FWHM for a Gaussian profile (Fan et al. 2003).

Next, each passband image is resampled using positional information, “`colc`” and “`rowc`”(real) in tsObj file, and “offsets wrt[2] reference colour”(`dcol` and `drow`; integer) and “bounding box”(`cmin` and `rmin`; integer) in “master mask” in fpAtlas file (see source code of readAtlasImages). Where “`colc`” and “`rowc`” are at the exact centre of the object in fpC coordinates, and $(\mathtt{cmin} + \mathtt{dcol}, \mathtt{rmin} + \mathtt{drow})$ is the fiducial point of atlas images in fpC coordinates. The typical errors of “`colc`” and “`rowc`” are $0.01 \sim 0.1$ pixel($0.004 \sim 0.04$ arcsec).

In the case of making $g{-}r$ 2D colourmaps without resampling r-band images, the preliminary position offset $(x0_{pg}, y0_{pg})$ of g-band pixels needed for $1\times$ g-band resampling in an atlas image coordinate is

$$\begin{array}{rcl} x0_{pg} & = & (\mathtt{colc}_g - \mathtt{col0}_g) - (\mathtt{colc}_r - \mathtt{col0}_r) \\ y0_{pg} & = & (\mathtt{rowc}_g - \mathtt{row0}_g) - (\mathtt{rowc}_r - \mathtt{row0}_r)\,, \end{array} \tag{3}$$

where $\mathtt{col0} = \mathtt{cmin} + \mathtt{dcol}$ and $\mathtt{row0} = \mathtt{rmin} + \mathtt{drow}$. And we consider the values $(d0_x, d0_y)$:

$$\begin{array}{rcl} d0_x & = & x0_{pg} - [x0_{pg}] \\ d0_y & = & y0_{pg} - [y0_{pg}] \end{array} \tag{4}$$

where $[x]$ is the floor function and $(d0_x, d0_y)$ indicates the distance from pixel grid and the resampled position of g-band pixels (That is, resampling is not required when $(d0_x, d0_y) = (0, 0)$).

---

[2] with reference to

Resampling only g-band images is not reasonable. Both r- and g-bands should be resampled and optimized. Then we determine the position offsets by $d0_x$,

$$\begin{array}{lcl} x0_{og} & = & x0_{pg} + (-d0_x/2) \\ x0_{or} & = & (-d0_x/2) \end{array} \qquad \text{for} \quad d0_x <= 0.5 \tag{5}$$

or

$$\begin{array}{lcl} x0_{og} & = & x0_{pg} + (1 - d0_x)/2 \\ x0_{or} & = & (1 - d0_x)/2 \end{array} \qquad \text{for} \quad 0.5 < d0_x \ , \tag{6}$$

and by $d0_y$,

$$\begin{array}{lcl} y0_{og} & = & y0_{pg} + (-d0_y/2) \\ y0_{or} & = & (-d0_y/2) \end{array} \qquad \text{for} \quad d0_y <= 0.5 \tag{7}$$

or

$$\begin{array}{lcl} y0_{og} & = & y0_{pg} + (1 - d0_y)/2 \\ y0_{or} & = & (1 - d0_y)/2 \end{array} \qquad \text{for} \quad 0.5 < d0_y \ . \tag{8}$$

These position offsets minimize declines in the resolution of r- and g-band images. The position offsets of u-, i- and z-bands, $x0_{ou}$, $x0_{oi}$ and $x0_{oz}$, are also derived by equation (5) or (6), and (7) or (8), replacing g with u, i or z. The $x0_{pu}$, $x0_{pi}$ and $x0_{pz}$ are calculated by equation (3), replacing g with u, i or z (Note that equation (4) is applied for the g-band only). In the case of $r - i$ 2D colourmaps, $x1_{oi}$, $y1_{oi}$, $x1_{or}$ and $y1_{or}$ are calculated using the same convention. When performing $1\times$ resampling, bilinear filtering is adopted.

Then we compute the surface brightness SB of each pixel on a $1\times$ resampled image and correct the reddening due to dust extinction in our Galaxy, using Schlegel, Finkbeiner & Davis (1998). The SDSS magnitudes m are derived by the following equations used in the SDSS photometric pipeline (PHOTO; Lupton et al. 2001),

$$f/f0 = N_{\rm cnt}/T_{\rm exp} \cdot 10^{0.4(v_{\rm aa} + v_{\rm kk} \cdot v_{\rm air})} \tag{9}$$

$$m_{\rm asinh} = -\frac{2.5}{\ln 10} \cdot \left\{ {\rm asinh}\left(\frac{f/f0}{2b} \right) + \ln b \right\} \tag{10}$$

$$m_{\rm Pogson} = -2.5 \cdot \log(f/f0) \tag{11}$$

where $N_{\rm cnt}$ is counts within an aperture on the atlas image, $T_{\rm exp}$ is exposure time in the fpC file, $v_{\rm aa}$, $v_{\rm kk}$ and $v_{\rm air}$ are zeropoint, extinction coefficient and airmass in the tsField file, and b is the asinh softening parameters. See the DR2 Photometric Flux Calibration page (http://www.sdss.org/dr2/algorithms/fluxcal.html) for details of computing magnitude from SDSS CCD images. Finally, we calculate 'pixel by pixel' K-corrected surface brightness using the `kcorrect.v3_2` library (Blanton et al. 2003). The same K-correction procedure is applied to each pixel in our galaxy based on the u,g,r,i and z colours of the pixel. The K-correction code uses several templates obtained as eigen vectors from the real SDSS spectra. During the fitting procedure, the code finds the bestfit out of the liner combinations of these template spectra. Therefore, the code does not try to break the age-metallicity degeneracy, but uses typical spectra with typical ages and metallicities to find the rest-frame colour of galaxies. Details of the K-correction code itself are written in Blanton et al. (2003).

The concentration index C_e is computed using an r-band image using elliptical apertures which eliminates the effect of the apparent axis ratio of the galaxy. The details of the effect and method of deriving the axis ratio and position angle are described in Yamauchi et al. (2005). To calculate the concentration index C_e for the ellipse, we consider area $A_e(a)$ of the ellipse of the semi-major axis a and axis ratio α, and the integrated flux $F_e(a)$ within $A_e(a)$. The Petrosian semi-major axis $a_{\rm P}$ for a given η is defined by

$$\eta = \frac{\{F_e(1.25a_{\rm P}) - F_e(0.8a_{\rm P})\}/\{A_e(1.25a_{\rm P}) - {\rm A_e(0.8a_P)}\}}{F_e(a_{\rm P})/A_e(a_{\rm P})}, \tag{12}$$

where we take $\eta = 0.2$, and the elliptical Petrosian flux $F_{\rm P}$ as

$$F_{\rm P} = F_e(ka_{\rm P}) \tag{13}$$

with k set equal to 2, following the SDSS definition (Strauss et al. 2002). The Petrosian half-, 60%- and 90%-light semi-major axes a_{50}, a_{60} and a_{90} are defined in such a way that the flux in the elliptical apertures of these semi-major axes are 50%, 60% and 90% of the elliptical Petrosian flux:

$$F_e(a_{50}) = 0.5F_{\rm P}, \ \ F_e(a_{60}) = 0.6F_{\rm P}, \ \ F_e(a_{90}) = 0.9F_{\rm P} \ . \tag{14}$$

We define our concentration index C_e by

$$C_e = a_{50}/a_{90} \ . \tag{15}$$

The axis ratio and the position angle used above are also adopted for the calculation of the radial colour gradient.

The radial colour gradients are based on our pixel-to-pixel K-corrected $g - r$ and $r - i$ 2D colourmap with Pogson magnitude. The regression lines to radial colour $(SB_g - SB_r)$ and $(SB_r - SB_i)$,

$$\begin{array}{lcl} (SB_g - SB_r) & = & t_{g\text{-}r} + CI_{g\text{-}r} \cdot \log(a/a_{60}) \\ (SB_r - SB_i) & = & t_{r\text{-}i} + CI_{r\text{-}i} \cdot \log(a/a_{60}), \end{array} \tag{16}$$

are calculated by linear least-squares fitting, and we define $CI_{g\text{-}r}$ and $CI_{r\text{-}i}$ as the radial colour gradient. The a is the equivalent distance from galaxy centre derived by the axis ratio and position angle. The Petrosian 60% flux radius corresponds to an effective radius with a pure de Vaucouleurs' profile. Generally the effective radius is used for the normalization of the radial colour gradient, but profile fitting is needed to calculate the effective radius. However, some E+A morphologies are somewhat disturbed and it is difficult to obtain a stable profile fit. Thus, we use the Petrosian 60% flux semi-major axis for stability of calculation. When this linear least-squares fitting is applied, the a/a_{60} of data points are restricted to $0.35 < a/a_{60} < 1.0$ to avoid a cusp in the galaxy centre and lower S/N regions in the outskirts. The minimum size of a_{60} in our samples applied to the colour gradient analysis is $2.83''$(7.14 pixels), and $a/a_{60} = 0.35$ corresponds to the diameter of $2.0''$, since the typical FWHM of the SDSS point-spread function is $\sim 1.5''$ (Shimasaku et al. 2001). We confirmed by our tests using a control sample that the effects of seeing on the derived colour gradients are not significant. The $({\rm FWHM}/2)/a_{60}$ v.s. $|CI_{g-r}|$ shows neither correlation (only 0.17 of correlation coefficient) nor systematic effect of seeing.

4 RESULTS

4.1 E+A Morphologies

Since E+A galaxies have experienced starburst truncation fairly recently ($<$ 1Gyr), E+A galaxies might still hold some traces in their morphology (e.g., dynamically disturbed signs). Therefore we might obtain some hint of the origins of E+A galaxies by examining their morphology.

First, we can confirm that E+A galaxies are centrally concentrated using concentration index C_e. In Figure 2, we show the distribution of C_e in 22 E+A galaxies. Galaxies that follow de Vaucouleurs' law give $C_e = 0.29$ and those with the exponential profile give 0.44, so C_e of early-type and late-type galaxies are clus-

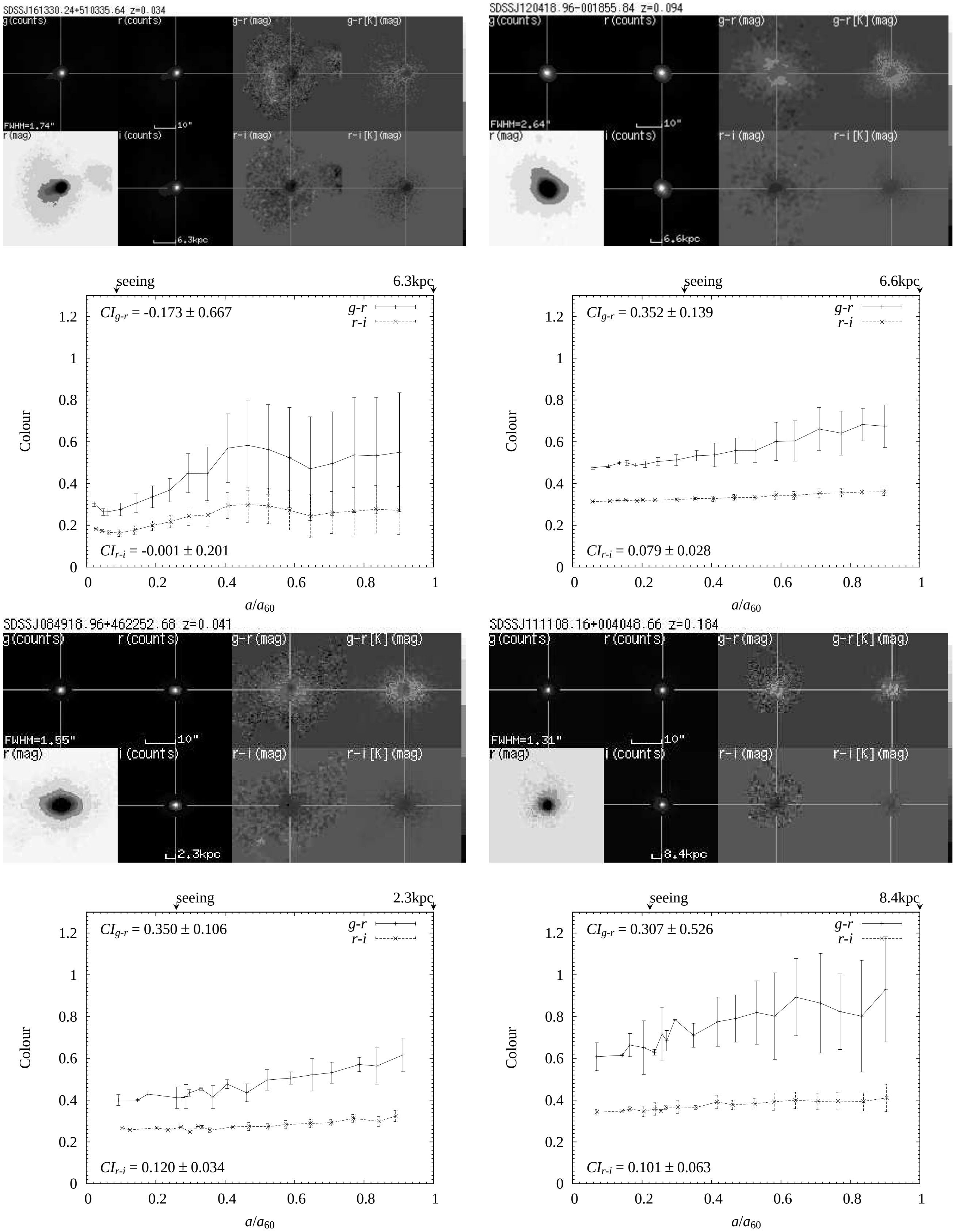

Figure 3. g-, r- and i-band images, $g-r$ and $r-i$ 2D colourmaps (*each top*) and the rest colour profiles (*each bottom*) of our all E+A galaxies. The error bars represent standard deviation of $g-r$ or $r-i$ values on sampling points. The details of explanation of image panels are inlaid in Figure 4. The panels are placed in ascending order with respect to D_{4000}. We numbered our E+As in this order, so this Figure includes No.1(*top left*), No.2(*top right*), No.3(*bottom left*) and No.4(*bottom right*) E+A galaxies. E+As with smaller D_{4000} tend to show positive slopes of radial colour gradients (bluer gradients toward the centre) and blue irregular patterns in 2D colourmaps. Meanwhile, those with larger D_{4000} show negative or flat slope and moderate property in 2D colourmap.

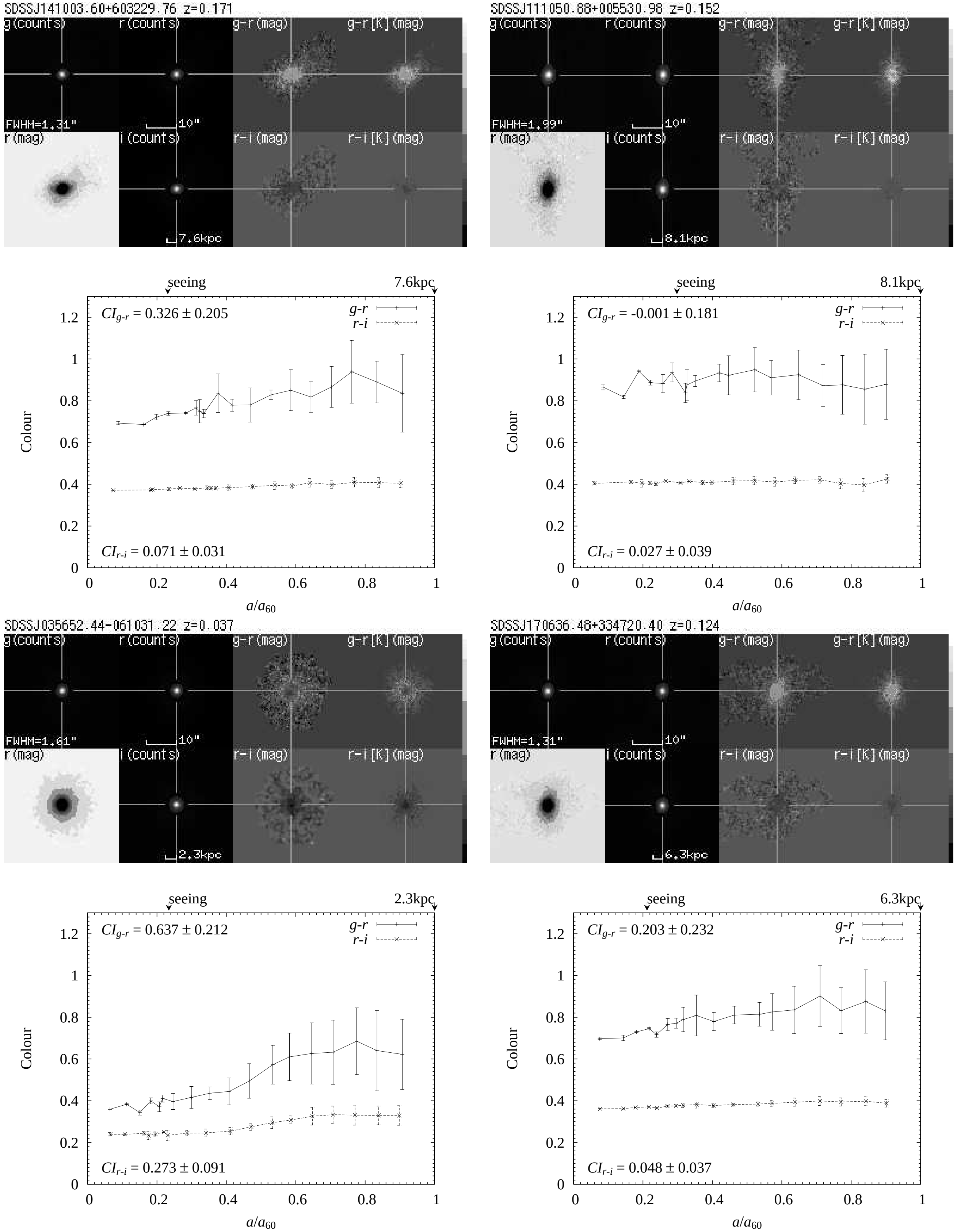

Figure 3 – *continued* No.5, No.6, No.7 and No.8 E+A galaxies

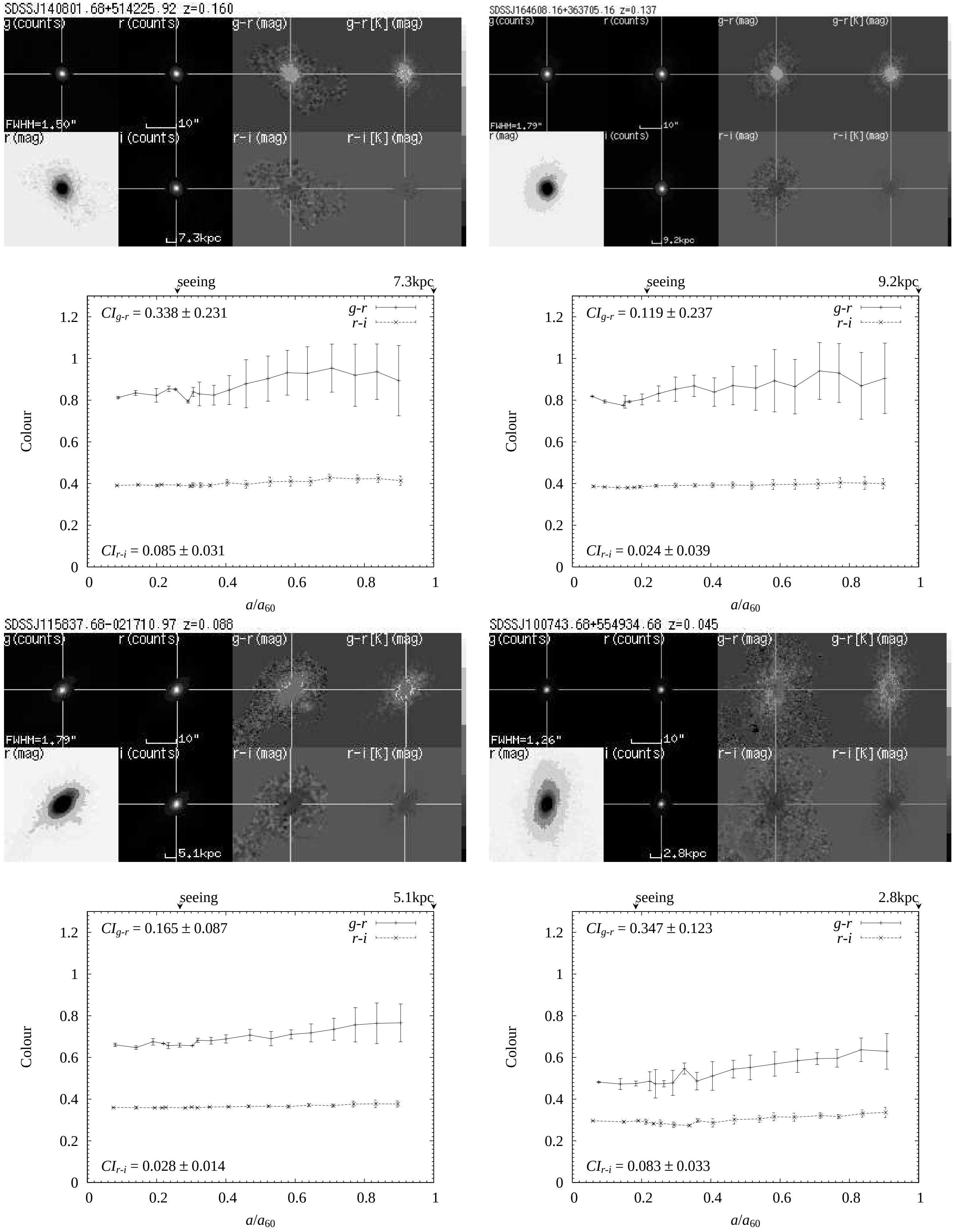

Figure 3 – *continued* No.9, No.10, No.11 and No.12 E+A galaxies

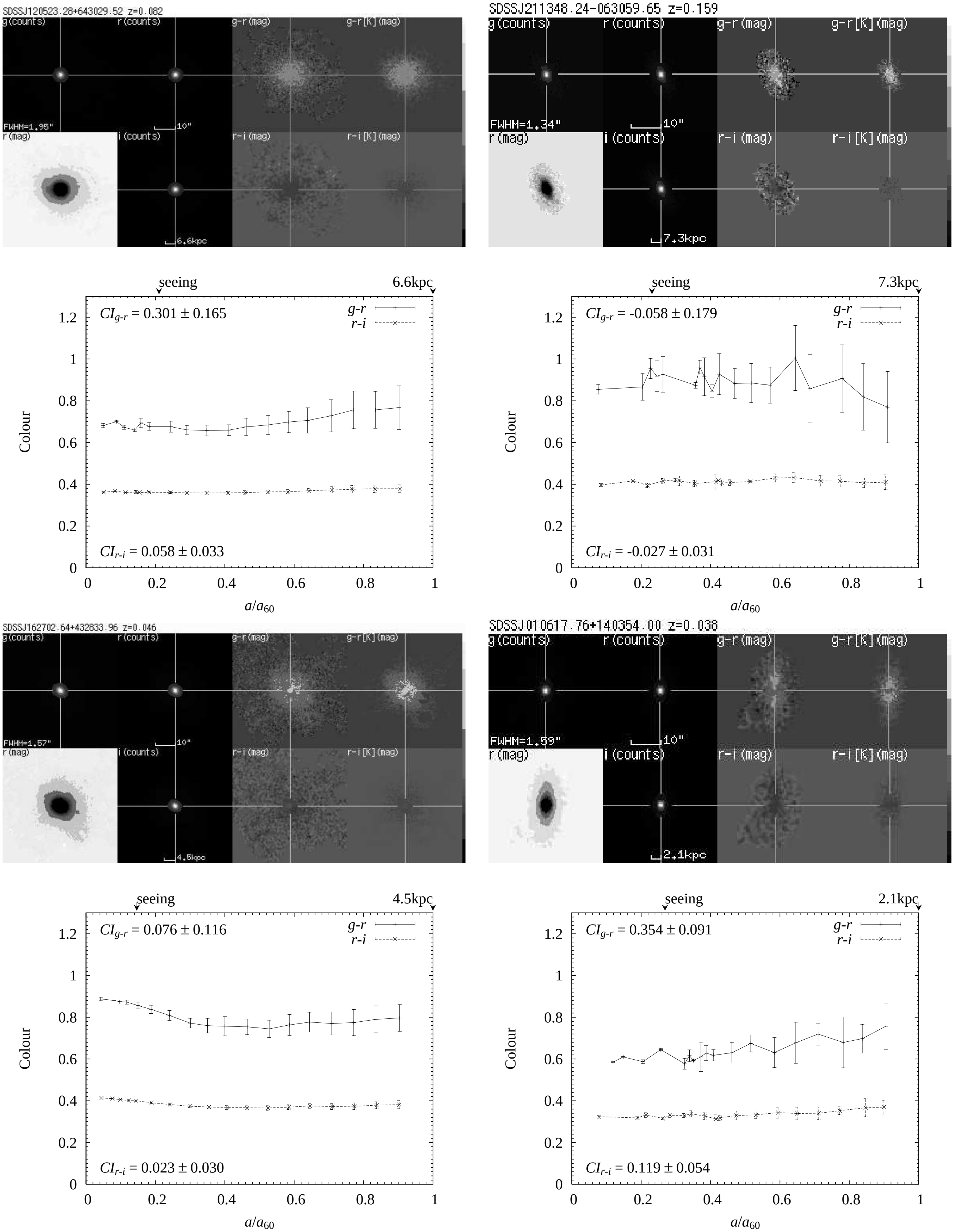

Figure 3 – *continued* No.13, No.14, No.15 and No.16 E+A galaxies

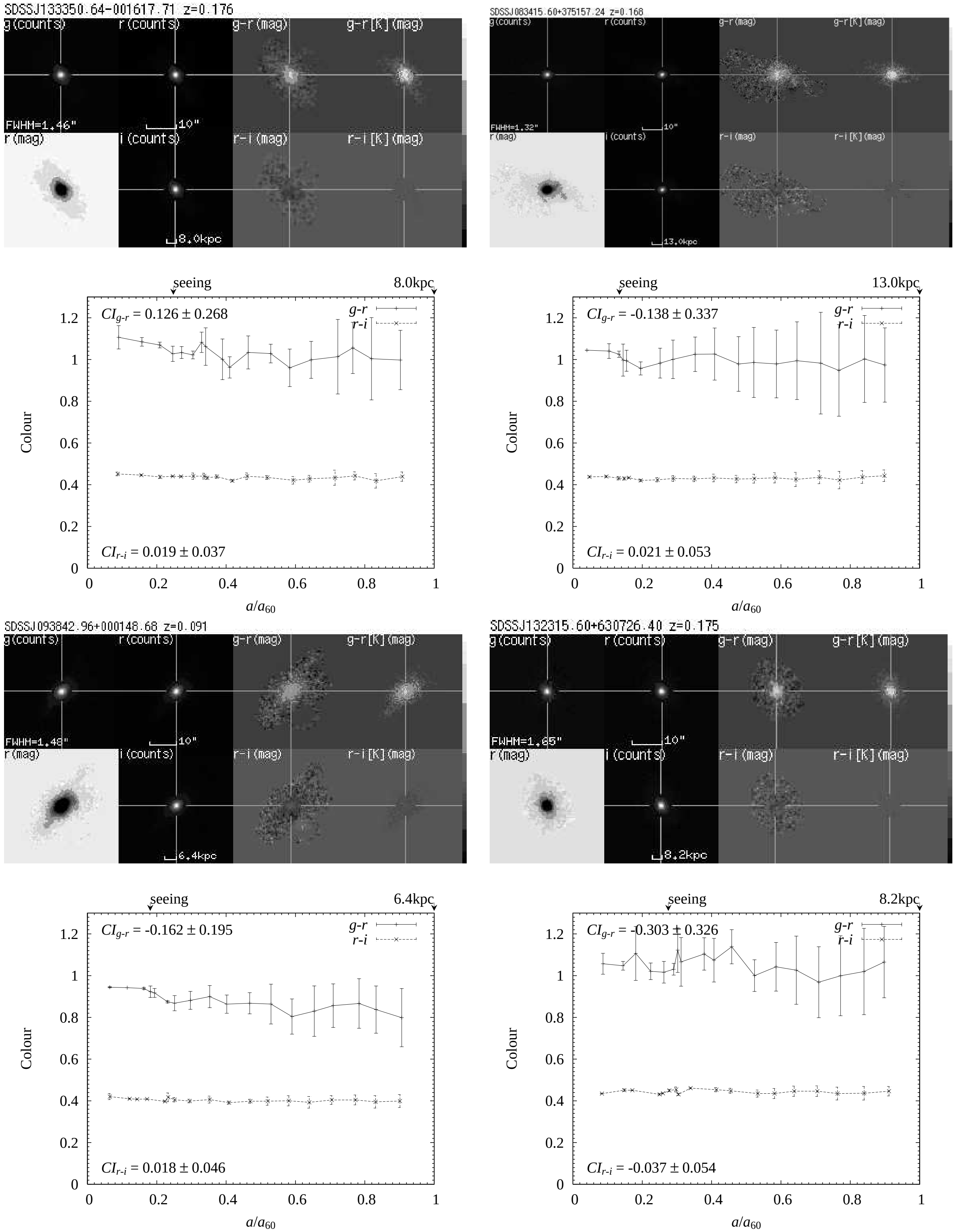

Figure 3 – *continued* No.17, No.18, No.19 and No.20 E+A galaxies

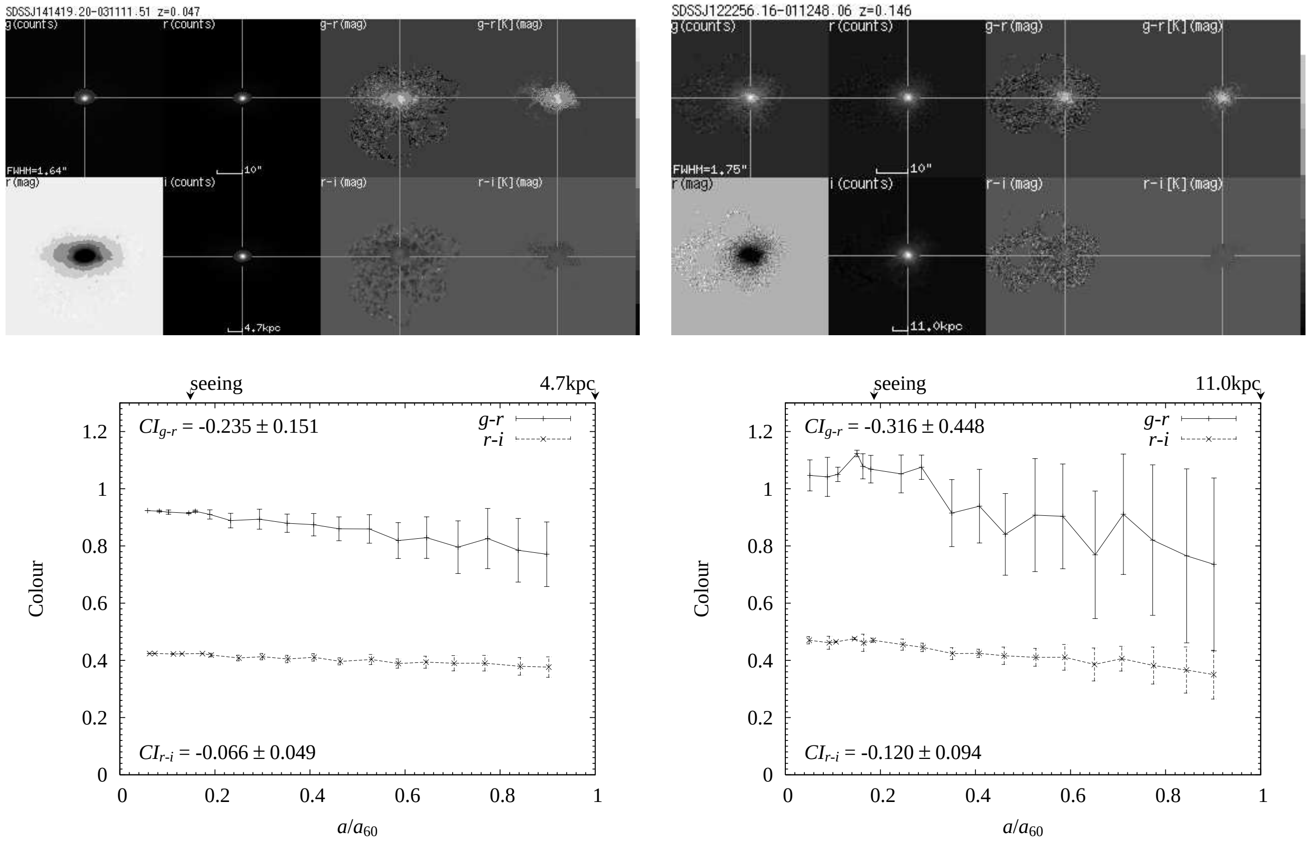

Figure 3 – *continued* No.21 and No.22 E+A galaxies

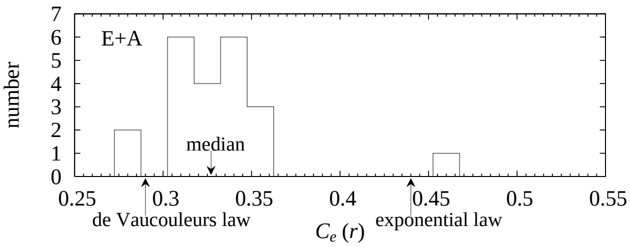

Figure 2. The distributions of concentration index C_e of 22 E+A galaxies. Galaxies that follow de Vaucouleurs' law give $C_e = 0.29$ and those with the exponential profile give 0.44. All our E+A galaxies except one are centrally concentrated galaxies.

tered on each point, respectively (See Yamauchi et al. 2005). C_e of 21 E+A galaxies are distributed in the same way as early-type galaxies, and the median $C_e = 0.33$ is a typical value of an E or S0 galaxy (Shimasaku et al. 2001; Strateva et al. 2001). Our visual inspection[3] of the SDSS images in Table 1 also shows that our E+A galaxies are predominantly early-type galaxies. We can interpret these results as a suggestion that all except one of our E+A galaxies are bulge-dominated systems.

We showed one of the most splendid SDSS E+A galaxies with a tidal feature in Figure 1. The SDSS imaging does not have high resolution (typical seeing size is $\sim 1.5''$) compared with the HST or 8m-class telescopes, but our 22 nearby or large E+A galaxies make a show of dramatic tidal tails or conspicuous disturbed morphologies. We present all r-band negative images of our E+A galaxies in Figure 3 on a logarithmic flux scale with 0% to 50%. The images in Figure 3 are placed in ascending order with respect to 4000Å break(D_{4000}), and we numbered our E+A galaxies according to this order. The physical size of a_{60} is displayed on the i-band image (right of the negative r-band image). To examine E+A morphologies, we present an image of a normal elliptical galaxy in Figure 4. Comparison between Figures 4 and 3 helps our examination of E+A morphologies. These 22 E+A galaxies exhibit a variety of disturbed features, ranging from what could visually be classified as a normal elliptical galaxy without disturbance (E+A No.7) to one with impressive tidal features (E+A No.1). We notice that at least half of our E+A galaxies have traces of merger/interaction, and exhibit tidal features or disturbed morphologies. If we observe our E+A galaxies with a higher resolution using an 8m-class telescope, we should be able to examine the details of these features and the fraction of E+A galaxies which leave traces of dynamically disturbed signs might increase.

4.2 2D Colour Properties: Radial Colour Gradients and Colour Morphologies

An example of $g-r$ and $r-i$ 2D colourmaps and their radial colour profiles of normal early-type galaxy are presented in Figure 4. The 3 positive images in the top left panel show g-, r- and i-band images by counts with seeing correction and resampling, and the 4 images on the right are $g-r$ and $r-i$ 2D colourmaps in asinh magnitude. The two rightmost panels of 2D colourmaps are pixel-to-pixel K-

---

[3] One of us (C.Y.) has performed a visual classification of the E+A galaxies in reference to the Third Reference Catalogue of Bright Galaxies (de Vaucouleurs et al. 1991, RC3).

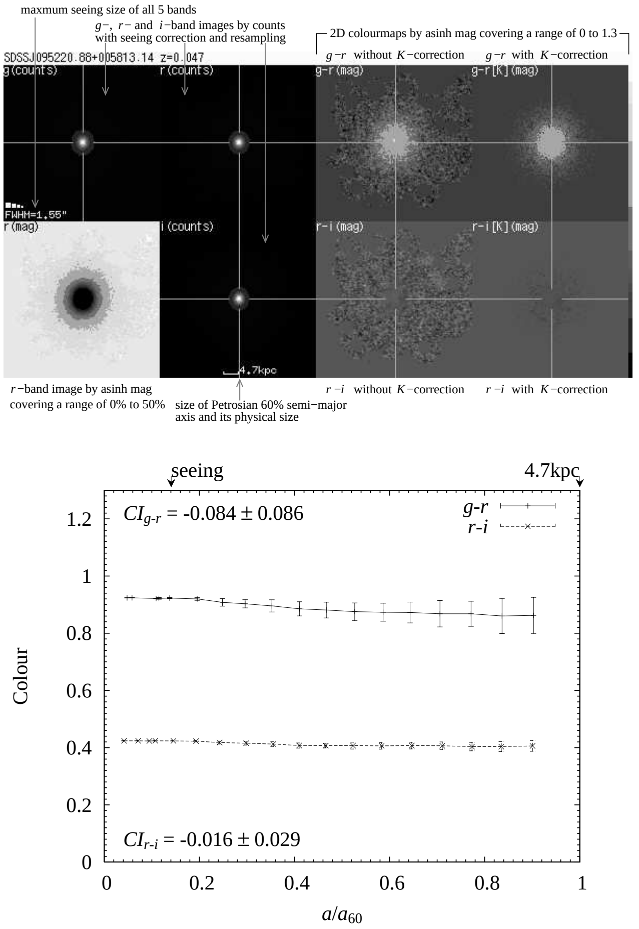

Figure 4. Example of g-, r- and i-band image, $g-r$ and $r-i$ 2D colourmaps (*top*) and the rest colour profiles (*bottom*) of a normal early-type galaxy. 2D colourmaps are based on asinh magnitude, but Pogson magnitude is used for colour profiles. The K-corrected 2D colourmaps are on the right, another has no K-correction applied. The error bars represent standard deviation of $g-r$ or $r-i$ values on sampling points within an annulus. The details of explanation are inlaid in the top panel. The 2D colourmaps of Elliptical galaxy are featureless, and many of them have moderate negative slope (redder gradients toward the centre) at $g-r$ and quite flat $r-i$ colour gradient.

corrected, while the others are not. The seeing sizes of all images are indicated in the g-band image. The bottom panel shows $g-r$ and $r-i$ radial colour profiles using Pogson magnitude, and seeing size(FWHM/2) and physical scale of a_{60} are displayed on the upper abscissa. In this figure, we inlay the explanation of images and 2D colourmap, and the same form is used in Figure 3, where we present all of our E+A galaxies.

The 2D colourmaps of elliptical galaxies are basically featureless, and the major difference between K-corrected and uncorrected is small. The radial colour profiles derived from 2D rest colour information also show moderate properties. Many elliptical galaxies have quite flat $r-i$ colour gradients and moderate negative slopes at $g-r$. Although there are many kinds of $g-r$ radial gradients in early-type galaxies, the positive slope (bluer gradients toward the centre) at $g-r$ profile is seldom seen.

Meanwhile, many of our E+A galaxies show mysterious 2D colourmaps and radial profiles. We present 2D colourmaps and radial profiles of all our E+A galaxies in Figure 3. The images and colour profiles in Figure 3 are placed in ascending order with respect to the 4000Å break(D_{4000}), and we have numbered our E+A galaxies according to this order. The slopes of $g-r$ radial profile of a number of E+A galaxies are positive (bluer gradients toward the centre) which is seldom seen in normal early-type galaxies. We list our 22 E+A galaxies in Table 1 with $CI_{g\text{-}r}$ and $CI_{r\text{-}i}$ results. It turns out that ∼63% of our E+A galaxies have a positive slope of radial $g-r$ colour gradient. In the case of the $r-i$ colour gradient, ∼77% of E+As have a positive slope. In addition, some E+A galaxies show an irregular pattern in their $g-r$ and $r-i$ 2D colourmap without K-correction — 'Colour Morphology' — asymmetrical and clumpy bluer region. The No.1, No.2 and No.3 E+A galaxies are especially conspicuous; the bluer regions are shown near the galaxy centre, but some of the bluest regions are placed slightly away from nucleus. However, the K-corrected 2D colourmaps tend to weaken this asymmetrical feature. We expect that such a region has a particular SED, and this may be a limit of K-correction by fitting template SEDs. These 'irregularities' on 2D colourmaps are observed in E+A galaxies with 'positive slopes'. But not all of the

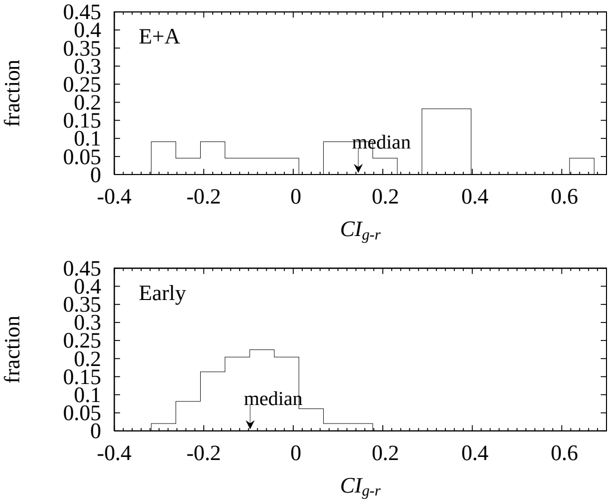

Figure 5. The histograms of $g-r$ radial colour gradient, showing E+A (*top*) and early-type (*bottom*) galaxies.

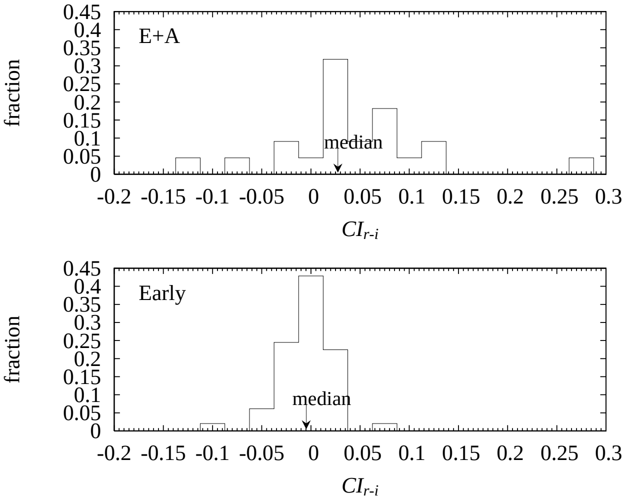

Figure 6. The histograms of $r-i$ radial colour gradient, showing E+A (*top*) and early-type (*bottom*) galaxies.

E+A galaxies with positive slopes necessarily have conspicuous irregularities on the 2D colourmap. That is, the E+A galaxies with ‘positive slopes’ of radial colour gradient tend to show irregular patterns on the 2D colourmap.

To compare the radial colour gradients of the E+A galaxies with those of normal early-type galaxies, the distributions of radial colour gradients $CI_{g\text{-}r}$ and $CI_{r\text{-}i}$ are displayed in Figures 5 and 6. It is clear that normal early-type galaxies have negative $g-r$ colour gradients, and almost all are placed within $-0.2 < CI_{g\text{-}r} < 0$, and $r-i$ colour gradients are concentrated at $CI_{r\text{-}i} \sim 0$. Each median is -0.10 and 0.005, respectively. On the other hand, $CI_{g\text{-}r}$ and $CI_{r\text{-}i}$ of E+A galaxies are dispersed, and galaxies with large positive slopes are obviously increased. Each median is also shifted to positive, 0.14 and 0.03, respectively. We then applied a Kolomogorov-Smirnov (K-S) two-sample test to find the probability that the two samples are drawn from the same parent distribution. The results show that $g-r$ and $r-i$ colour gradient distributions of E+A are different from those of early-type galaxies with a more than 99.99% significance level.

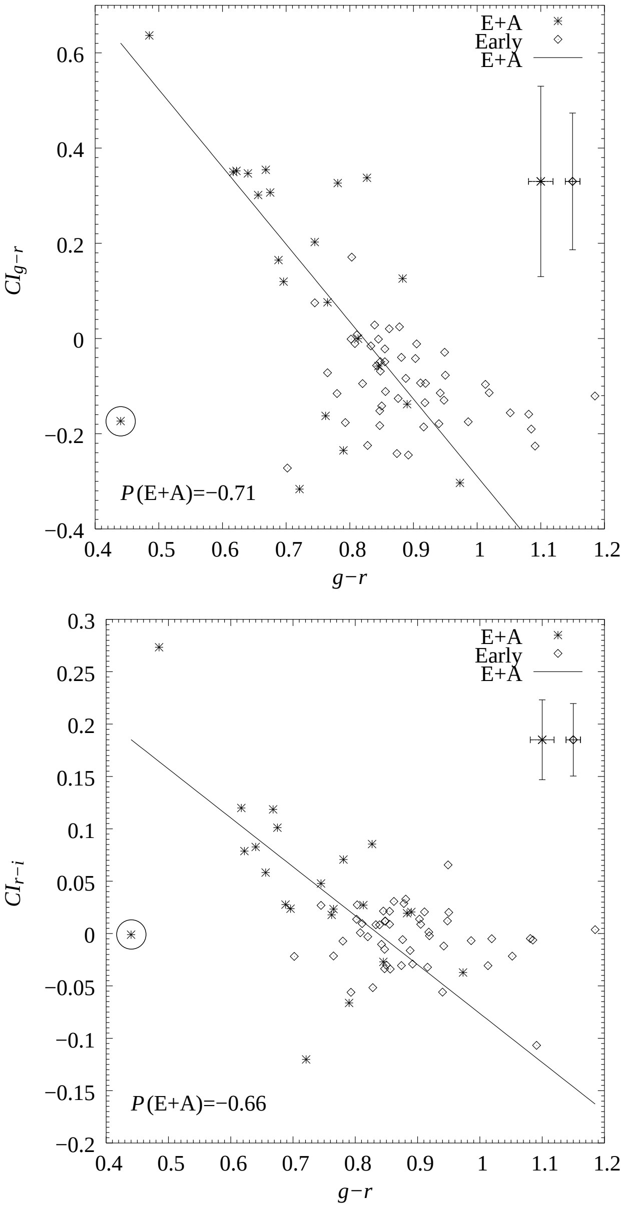

Figure 7. The $g-r$ radial colour gradient plotted against $g-r$ rest colour (*top*) and $r-i$ radial colour gradient plotted against $g-r$ rest colour (*bottom*), showing 22 E+A and 49 early-type galaxies. E+A and early-type galaxies are plotted using asterisks and open lozenges, respectively. The coefficient P on the bottom left is the Spearman linear correlation coefficient, and the solid line represents a linear least-squares fit using E+A data points. The circled asterisks are No.1 E+A galaxy rejected for P and linear least-squares fit. Error bars at the top right are typical errors of the observational data.

4.3 Comparison between Radial Colour Gradient and Other Photometric/Spectroscopic Properties

We showed that E+A galaxies have interesting radial colour gradients. Comparison between radial colour gradient and other photometric/spectroscopic properties may provide a clue to the E+A evolution scenario.

Figures 7 and 8 show the relation between radial colour gradients CI and rest $g-r$ or $r-i$ colours. Observed colours in this paper are shifted to the restframe using the K-correction software (`v3_2`) by Blanton et al. (2003). Our 22 E+A and 49 early-type galaxies are plotted using asterisks and open lozenges, respectively. The error bars on the top right indicate a typical error. Coefficient P on the bottom left is the Spearman linear correlation coefficient, and the solid line represents a linear least-squares fit using E+A data points. A data point with an open circle is No.1 E+A galaxy rejected for P and linear least-squares fit, since the errors of $CI_{g\text{-}r}$ and $CI_{r\text{-}i}$ are too large (0.67 and 0.20, respectively). We expect that E+A galaxy No.1 has too heavy a disturbance feature to permit calculation of the appropriate Petrosian radius. We can find obvious correlations of $P \sim -0.7$ level between radial colour gradients and colours. But some of the derived regressions appear to rely heavily on the one point, $g-r = 0.48$ E+A galaxy. So we have examined the Spearman linear correlation coefficient P with $0.5 < g-r$ points only in Figure 7, and gotten $P = -0.62$ and -0.59, respectively. On the other hand, the early-type galaxies show only $P \sim -0.32$ at the maximum absolute value in these diagrams. Therefore, derived P of E+As which indicate correlations between colour gradients and colours have some dependence upon the one point; however, it is not a prime factor. The results also support the idea that the photometric properties of E+A are significantly different from those of early-type galaxies.

Next, we compare the radial colour gradients with spectroscopic properties. In Figure 9, we plot radial colour gradients against the 4000Å break (D_{4000}) which is sensitive to old stellar populations. Symbols and rejections are the same as in previous figures. This diagram evidently indicates the correlation between radial colour gradients and the 4000Å break. Early-type galaxies show less than $|P| \sim 0.2$ level correlations like those of colour gradients and colours. But normal early-type galaxies are not placed under the regression line, different from plots of colour gradients against colours. D_{4000} is shown to separate the two populations more clearly than the broad-band colours.

To examine the relation between radial colour gradients and the amount of young A-type stars, we plot radial colour gradients against Hδ EW in Figure 10. Symbols are the same as in previous figures. Compared with the case of D_{4000}, we cannot find a tight correlation. However, these panels show a trend for E+A galaxies with large positive slope of radial colour gradient to show strong

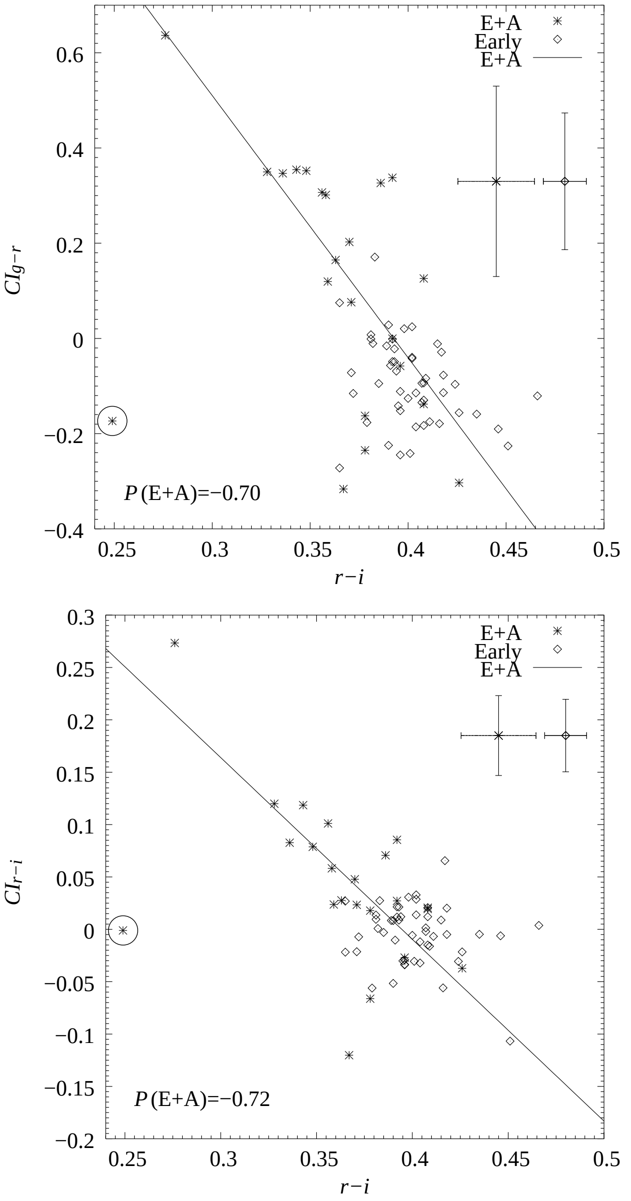

Figure 8. The $g-r$ radial colour gradient plotted against $r-i$ rest colour (*top*) and $r-i$ radial colour gradient plotted against $r-i$ rest colour (*bottom*), showing 22 E+A and 49 early-type galaxies. E+A and early-type galaxies are plotted using asterisks and open lozenges, respectively. The coefficient P at the bottom left is the Spearman linear correlation coefficient, and the solid line represents a linear least-squares fit using E+A data points. The circled asterisks are No.1 E+A galaxy rejected for P and linear least-squares fit. Error bars at the top right are typical errors of the observational data.

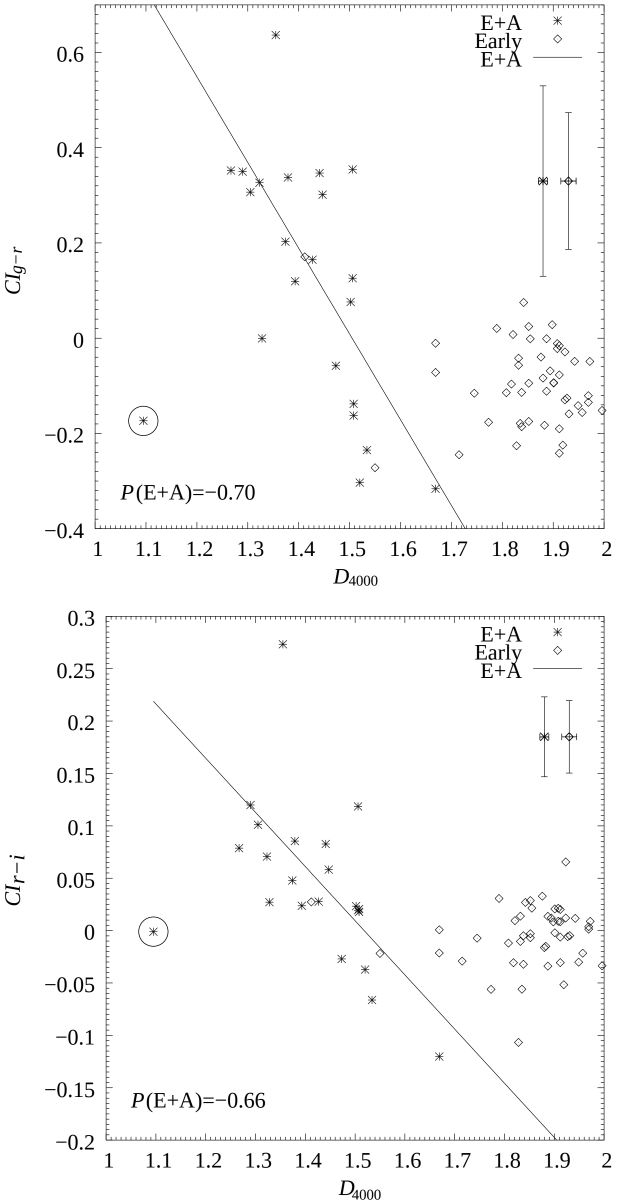

Figure 9. The $g-r$ radial colour gradient plotted against D_{4000} (*top*) and $r-i$ radial colour gradient plotted against D_{4000} (*bottom*), showing 22 E+A and 49 early-type galaxies. E+A and early-type galaxies are plotted using asterisks and open lozenges, respectively. Coefficient P on the bottoms left is the Spearman linear correlation coefficient, and the solid line represents a linear least-squares fit using E+A data points. The circled asterisks are No.1 E+A galaxy rejected for P and linear least-squares fit. Error bars at the top right are typical errors of the observational data.

Hδ EWs. However, this result might be affected by the cut-off of $a/a_{60} < 0.35$ for measuring radial colour gradient.

4.4 Evolution Scenario for E+A Radial Colour Gradients

In this subsection, we compare SED models and observational quantities to find out the evolution scenario for E+A radial colour gradients. Using the GISSEL model by Bruzual & Charlot (2003), we simulated three representative star formation histories following Goto (2003): (i) The *Burst* model, which has an instantaneous starburst (with a duration of 1 Gyr) at the beginning and no star formation thereafter. (ii) *Constant* star formation. (iii) *Exponentially* decaying star formation (with $\tau = 1$ Gyr). In all three models, we use the Salpeter initial mass function (Salpeter 1955). Figure 11 plots Hδ EWs against time (or galaxy age) for the three models. The dot-dashed, solid and dotted lines show the models with instantaneous burst, constant star formation and exponentially decaying star formation rate. The burst model has a strong Hδ EW right after its truncation at 1 Gyr. However, its Hδ EW declines rapidly, and becomes less than 3Å at 1 Gyr after the truncation. The expo-

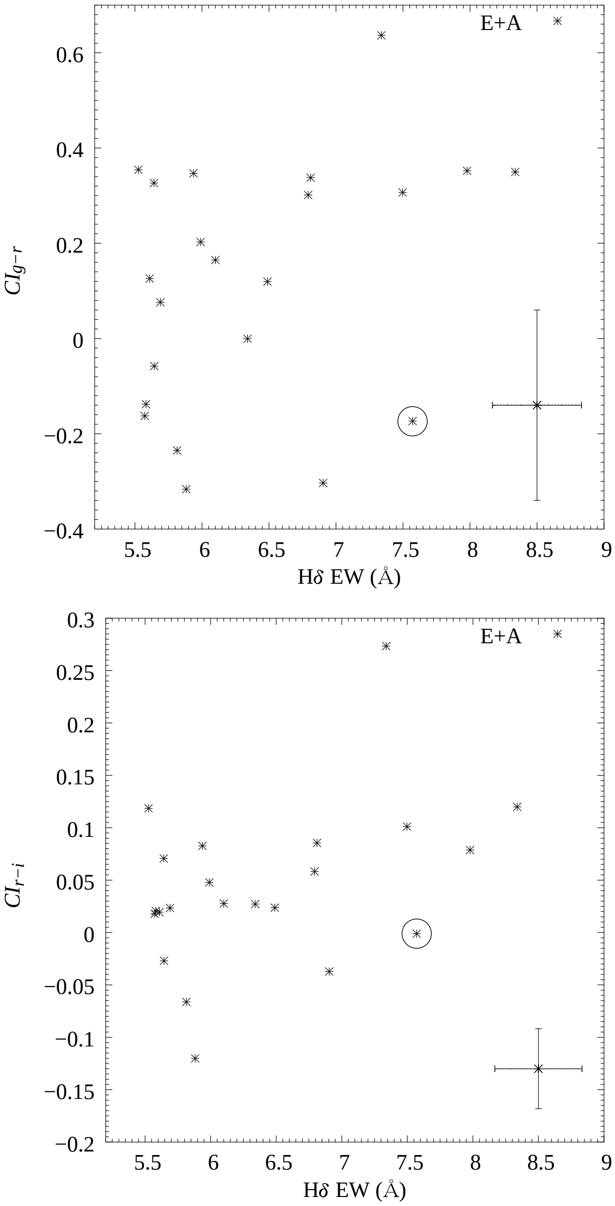

Figure 10. The $g-r$ radial colour gradient plotted against Hδ EWs (*top*) and $r-i$ radial colour gradient plotted against Hδ EWs (*bottom*), showing 22 E+A galaxies. The circled asterisks are No.1 E+A galaxy. Error bars at the bottom right are typical errors of the observational data.

nentially decaying model maintains a strong Hδ for a longer time. Its Hδ EW becomes 3Å in 5 Gyrs. The constantly star-forming model maintains a large Hδ EW (>6Å) beyond 13 Gyr. Although shown here for a comparison purpose, we omit the constantly star-forming model from our main discussion, since our E+A galaxies are selected to have no on-going star formation activity.

We compare the models and the data on the Hδ EW v.s. D_{4000} plane in Figure 12. A caveat, however, is that models become less accurate on the plane since both Hδ EW and D_{4000} are more difficult quantities to reproduce than broad band colours. For models, we use Hδ EWs given in the GISSEL model, which were measured using the flux between 4083.50 and 4122.25Å. This is essentially the same window as used to measure Hδ EWs from the observational data between 4082 to 4122Å. For D_{4000}, the SED

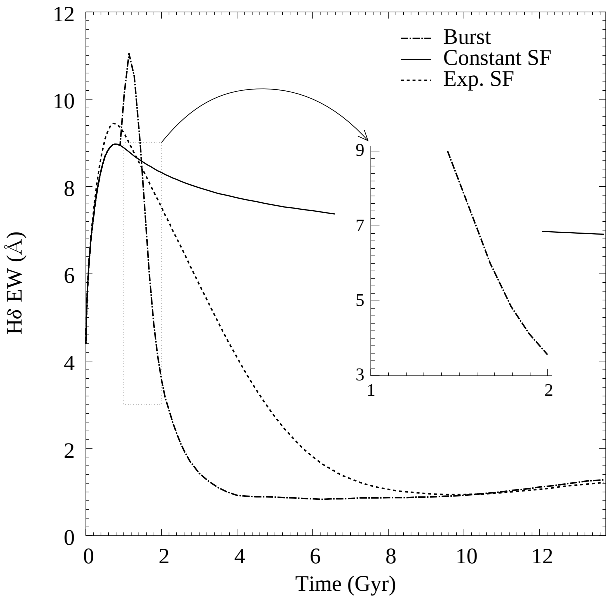

Figure 11. Hδ EWs are plotted against time (age) for three star formation histories with the GISSEL model. The dot-dashed, solid and dotted lines show the models with instantaneous burst, constant star formation and exponentially decaying star formation rate. The models in this figure assume Salpeter IMF and solar metallicity. The inlaid panel is an enlarged plot of the burst model with $3 < \mathrm{H}\delta\ \mathrm{EW} < 9$.

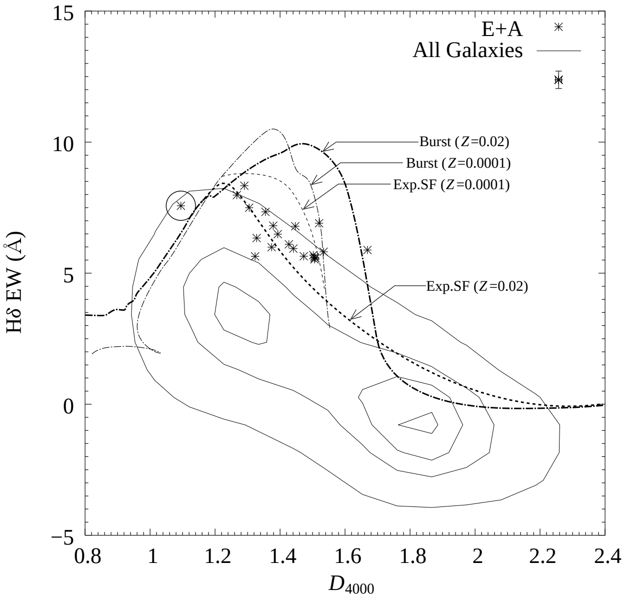

Figure 12. Hδ EWs are plotted against D_{4000} for the models with $Z = 0.0001(0.5\%\ \mathrm{solar})$ and $Z = 0.02(\mathrm{solar})$. Star formation histories are the burst and exponentially decreasing, shown by the dot-dashed and dotted, respectively. Observational data are plotted using asterisks. The circled asterisk is No.1 E+A galaxy. Error bars at the top right are typical errors of the observational data. The contours show the distribution of all DR1 94770 galaxies in Goto (2003).

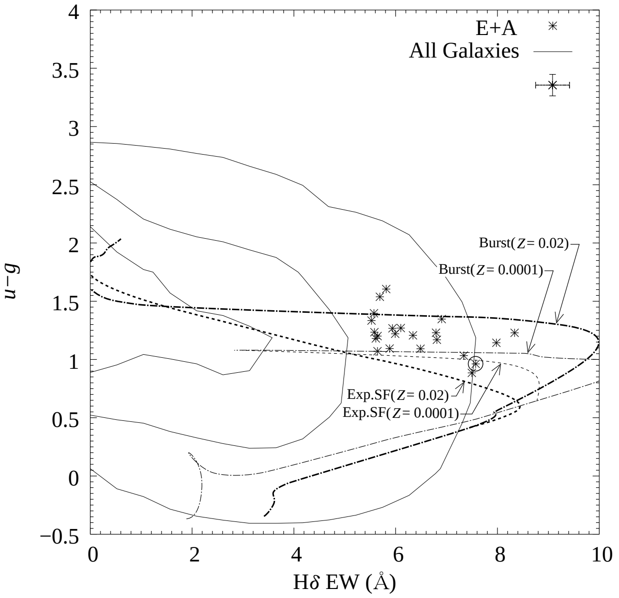

Figure 13. The $u-g$ colour is plotted against Hδ EWs for the models with $Z = 0.0001$(0.5% solar) and $Z = 0.02$(solar). The dot-dashed and dotted lines are for the models with instantaneous burst and exponentially decaying star formation rate. Observational data are plotted using asterisks. The circled asterisk is No.1 E+A galaxy. Error bars at the top right are typical errors of the observational data. The contours show the distribution of all DR1 94770 galaxies in Goto (2003).

models uses the flux ratio of the 3750-3950Å window to the 4050-5250Å window (Bruzual 1983). Observationally, D_{4000} is measured using the ratio of the flux in the 3751-3951Å window to that in the 4051-4251Å (Stoughton et al. 2002). We regard these two D_{4000} measurements as essentially the same.

In Figure 12, the dot-dashed and dotted lines are for the models with the instantaneous burst and the exponentially decaying star formation rate. We subtracted 1Å from the model Hδ EWs to compensate for possible stellar absorption. Different line widths are for two different metallicities ($Z = 0.001$ and 0.02). Goto (2003) showed that the models might have a slight shift toward larger D_{4000} and Hδ directions, compared with the distribution of all the observed galaxies. In the models, emission fillings are not included, and might be a factor in gaps between observational data and the model. However, the behavior of the models on this plane well reproduce expected behavior of galaxies, in the sense that star-forming galaxies evolve into large D_{4000} and small Hδ EWs. Therefore, we regard the qualitative interpretation based on the models as valid. Observed data of E+A galaxies are plotted using asterisks, and we find for the most part that our E+A galaxies are located under a single evolution track. But it is uncertain whether these E+A galaxies run along the track of instantaneous burst or not, since models might have a slight shift reported by Goto (2003).

Goto (2003) also reported that it is more difficult to reproduce emission lines with the current version of the model. The model gives the amount of Lyα photons, so we could use it to estimate the amount of Balmer or [OII] line emissions. However, we found that the uncertainty in this process was too large to produce a realistic value comparable with the observational values (We do not know the escaping factor of Lyα photons, etc.). We found a qualitative agreement in the long scale, but in the liner scale, the model [OII] EW (or Hα EW) was far from agreement. On the other hand, the $u-g$ colour is preferable for examination of on-going star formation since it shows better agreement between the SED models and the observation data. In Figure 13, we plot $u-g$ against Hδ EW for the two models and the observational data. Symbols are the same as previous figures. The model $u-g$ colour depends on metallicity to some extent, showing bluer $u-g$ colour with decreasing metallicity. Our E+A galaxies are distributed between the instantaneous burst model with $Z = 0.001$ and that with solar metallicity. Neither of the exponentially decaying models can explain the observed data. This indicates that E+A galaxies are in a post-starburst phase, and cannot be explained by more normal star formation histories.

If the burst model is assumed, our young E+A galaxies with Hδ EW $\sim$ 8Å evolve into those with Hδ EW $\sim$ 5Å within $\sim$300 Myr by Figure 11. Our radial colour gradient correlates with D_{4000} in Figure 9, and E+A galaxies with large positive slopes of radial colour gradient tend to show strong Hδ EWs (Figure 10). Our E+A galaxies are placed under a single track on the D_{4000} - Hδ EW plane; therefore, we can interpret these results as some E+A metamorphosis of large positive slopes into flat or negative slopes of radial colour gradients within the time scale. Taken together, our observational results suggest that E+A galaxies have positive colour gradients, large Hδ EW and small D_{4000} at the beginning, then evolve into negative colour gradients, small Hδ EW and large D_{4000}. It is revealing that the morphological quantity, colour gradients, correlates well with spectral properties such as Hδ EW and D_{4000}.

5 DISCUSSION

Based on SDSS broad-band imaging, we investigated spatial properties such as morphologies, 2D colour properties and radial colour gradients of E+A galaxies. In this section, we discuss physical implications and the relevance of our results to other E+A-related studies.

The concentration index, C_e, of our E+A galaxies was distributed like early-type galaxies, and our visual inspection of the SDSS images also showed that our E+A galaxies are predominantly early-type galaxies. We can interpret these results as a suggestion that all of our E+A galaxies are bulge-dominated systems. Although E+As with disk-like morphologies have sometimes been found in previous observations (Couch et al. 1994, 1998; Dressler et al. 1994, 1999; Oemler, Dressler & Butcher 1997; Smail et al. 1997; Chang et al. 2001), it is not surprising if previous samples were contaminated by Hα-emitting galaxies. Perhaps since we selected 22 E+A galaxies with strict spectroscopic criteria, ‘without Hα nor [OII] emission’, our 22 E+A galaxies are all bulge-dominated. Our results are also consistent with those by Quintero (2004) and Blake et al. (2004).

These findings have important implications for the physical origin of E+A galaxies when compared with theoretical simulations. It has long been known that an elliptical galaxy can be a final product of major merging (e.g., Barnes & Hernquist 1992), quite possibly accompanied by a tidal tail feature in its early stage. In a more detailed major merger model, Bekki (1998) showed that ancestral equal-mass galaxies are completely destroyed so as to form a spheroid that looks more like an elliptical galaxy, and merging of two unequal-mass spirals is finally transformed into one S0 galaxy that has a flattened oblate spheroid. We noticed that at least half of our E+A galaxies show tidal features or disturbed morphologies. Thus not only disturbed morphologies but also E/S0 morphologies

Table 1. The list of E+A galaxies. The numbers are labeled in ascending order with respect to D_{4000}. The digits in Name represent R.A. and Dec., for example, R.A. and Dec. of Name SDSSJ010617.76+140354.00(No.16) are 01:06:17.76 and +14:03:54.00, respectively. The unit of a_{60} and line EWs are arcsec and Å, respectively. The morphological type $T = 0, 1, 2, 3, 4, 5, 6$ and -1 represent E,S0,Sa,Sb,Sc,Sdm,Im and unclassified, respectively.

No.	Name	z	M_r	$u-g$	$g-r$	$r-i$	a_{60}	D_{4000}	Hδ EW	Hα EW	[OII] EW	C_e	T	$CI_{g\text{-}r}$	$CI_{r\text{-}i}$
16	SDSSJ010617.76+140354.00	0.038	-19.76	1.33	0.67	0.34	2.96	1.51	5.53±0.32	2.10±0.08	-0.13±-0.02	0.28	1	0.35±0.09	0.12±0.05
7	SDSSJ035652.44-061031.22	0.037	-19.85	1.03	0.48	0.28	3.43	1.35	7.34±0.41	2.39±0.10	-0.46±-0.05	0.32	0	0.64±0.21	0.27±0.09
18	SDSSJ083415.60+375157.24	0.168	-23.10	1.23	0.89	0.41	4.93	1.51	5.58±0.23	0.74±0.02	-0.22±-0.03	0.32	-1	-0.14±0.34	0.02±0.05
3	SDSSJ084918.96+462252.68	0.041	-20.88	1.23	0.62	0.33	3.00	1.29	8.34±0.27	1.91±0.05	-1.17±-0.08	0.31	1	0.35±0.11	0.12±0.03
19	SDSSJ093842.96+000148.68	0.091	-21.84	1.40	0.76	0.38	4.07	1.51	5.57±0.47	1.15±0.04	-1.62±-0.21	0.36	-1	-0.16±0.19	0.02±0.05
12	SDSSJ100743.68+554934.68	0.045	-20.88	1.27	0.64	0.34	3.44	1.44	5.94±0.32	1.57±0.05	-2.06±-0.20	0.28	1	0.35±0.12	0.08±0.03
6	SDSSJ111050.88+005530.98	0.152	-22.22	1.21	0.81	0.39	3.34	1.33	6.34±0.32	1.28±0.05	-0.94±-0.13	0.33	1	-0.00±0.18	0.03±0.04
4	SDSSJ111108.16+004048.66	0.184	-22.32	0.89	0.68	0.36	2.95	1.30	7.50±0.47	1.60±0.08	-0.57±-0.08	0.36	1	0.31±0.53	0.10±0.06
11	SDSSJ115837.68-021710.97	0.088	-22.11	1.27	0.69	0.36	3.35	1.43	6.10±0.28	1.75±0.07	0.69±0.09	0.34	-1	0.16±0.09	0.03±0.01
2	SDSSJ120418.96-001855.84	0.094	-22.74	1.14	0.62	0.35	4.10	1.27	7.98±0.27	2.11±0.06	-1.18±-0.07	0.31	-1	0.35±0.14	0.08±0.03
13	SDSSJ120523.28+643029.52	0.082	-22.78	1.23	0.66	0.36	4.64	1.45	6.79±0.29	1.78±0.05	0.91±0.09	0.31	-1	0.30±0.16	0.06±0.03
22	SDSSJ122256.16-011248.06	0.146	-21.74	1.09	0.72	0.37	4.69	1.67	5.88±1.42	1.19±0.05	0.61±0.40	0.45	2	-0.32±0.45	-0.12±0.09
20	SDSSJ132315.60+630726.40	0.175	-21.94	1.35	0.97	0.43	3.00	1.52	6.90±0.93	1.11±0.07	1.56±0.36	0.35	1	-0.30±0.33	-0.04±0.05
17	SDSSJ133350.64-001617.71	0.176	-22.35	1.18	0.88	0.41	2.94	1.51	5.61±0.49	2.21±0.14	0.71±0.15	0.31	1	0.13±0.27	0.02±0.04
9	SDSSJ140801.68+514225.92	0.160	-22.34	1.17	0.83	0.39	2.88	1.38	6.81±0.37	-0.12±-0.00	0.51±0.07	0.33	1	0.34±0.23	0.09±0.03
5	SDSSJ141003.60+603229.76	0.171	-22.76	1.07	0.78	0.39	2.83	1.32	5.64±0.25	0.67±0.05	-1.08±-0.07	0.31	-1	0.33±0.21	0.07±0.03
21	SDSSJ141419.20-031111.51	0.047	-21.37	1.60	0.79	0.38	5.53	1.53	5.81±0.34	0.33±0.01	-1.11±-0.18	0.34	-1	-0.24±0.15	-0.07±0.05
1	SDSSJ161330.24+510335.64	0.034	-20.06	0.96	0.44	0.25	9.98	1.09	7.57±0.29	0.54±0.02	1.10±0.21	0.36	-1	-0.17±0.67	-0.00±0.20
15	SDSSJ162702.64+432833.96	0.046	-21.75	1.54	0.77	0.37	5.38	1.50	5.69±0.22	0.67±0.01	-1.41±-0.12	0.32	-1	0.08±0.12	0.02±0.03
10	SDSSJ164608.16+363705.16	0.137	-22.45	1.09	0.70	0.36	4.15	1.39	6.49±0.46	1.12±0.03	-0.35±-0.04	0.35	-1	0.12±0.24	0.02±0.04
8	SDSSJ170636.48+334720.40	0.124	-22.06	1.22	0.74	0.37	3.08	1.37	5.99±0.39	0.34±0.02	-0.84±-0.10	0.32	-1	0.20±0.23	0.05±0.04
14	SDSSJ211348.24-063059.65	0.159	-22.11	1.20	0.84	0.40	2.90	1.47	5.64±0.51	0.96±0.03	-2.32±-0.56	0.33	1	-0.06±0.18	-0.03±0.03

of our unalloyed E+A sample indicate possibilities of a merger origin of E+A galaxies, and we can expedite the following discussion smoothly.

We found irregular ‘Colour Morphologies’ – asymmetrical and clumpy patterns – at the centre of the $g-r$ and $r-i$ 2D colourmaps of E+A galaxies without K-correction. The HST observations of the five bluest E+A galaxies with $z \sim 0.1$ by Yang et al. (2004) show the presence of asymmetric components in the residual images obtained by subtraction of the smooth and symmetric model images from the data. The physical scale of the asymmetric components of the HST observation is comparable to that of our asymmetrical/clumpy pattern in the 2D colourmap. We expect that these irregularities of residual images and our 2D colourmap basically have the same origin, and one possible interpretation is that they are fluctuations created during the merger/interaction event, which also caused the central post-starburst phase.

Our results showed that more than half of our E+A galaxies exhibit the positive radial $g-r$ and $r-i$ colour gradients. The results of $g-r$ radial colour gradients are in good agreement with a long-slit spectroscopic observation of 21 E+A galaxies by Norton et al. (2001) who found that young stellar populations of E+A galaxies are more centrally concentrated than the older populations. Although Bartholomew, Rose & Gaba (2001) reported that E+A galaxies on average tend to have slightly bluer radial gradients toward the centre than the normal early-type galaxies, these E+A galaxies are detected in rich clusters and their spectroscopic criteria ($3 < \langle \mathrm{H}\delta\gamma\beta \text{ EW} \rangle$ and $-5 < [\mathrm{OII}]$ EW) are less strict than ours. It is perhaps difficult to compare our E+A galaxies with those selected with different criteria in different environments. However, we can find the same tendency for a substantial number of E+A galaxies to have a positive slope of radial colour gradient and for our strict spectroscopic criteria to produce clearer results of a K-S test (with a more than 99.99% significance level). Theoretically, models of interacting gas-rich spirals suggest that the most common result of such tidal perturbations is indeed to drive a large fraction of interstellar material close to the centre of each galaxy; the shocked gas robbed of its angular momentum flows inward (Barnes & Hernquist 1992). Mihos, Richstone & Bothun (1992) showed not only that the vast majority of the star formation arises in central regions of the merging galaxies, but also that flybys which involve prograde disks cause significant centralized starburst. Especially, Mihos & Heanquist (1994) numerically simulated galaxy mergers and predicted colour gradients in such systems. In their Fig.7, they show that the colour gradient of merger remnants changes the slope of colour gradient from positive to negative during 1-5 Gyr after the burst in a way qualitatively similar to our Fig.3. The agreement adds more credibility to the notion of the merger/interaction origin of E+A galaxies, and further justifies our interpretation of change of the slope as an evolutionary sequence. In summary, our findings of positive $g-r$ radial colour gradients of E+A galaxies are consistent with the merger/interaction origin of E+A galaxies.

We found a tight correlation between radial colour gradients and 4000Å break. We also found that E+A galaxies follow a single evolution track on the D_{4000} - Hδ EW plane (in Figure 12). Taken all together, these results can be interpreted in an evolutionary sequence where E+A galaxies change their slope from positive to negative, and they also change irregular into moderate of 2D colourmap during the time scale of ∼300 Myr. It is revealing that E+A galaxies show morphological metamorphosis (change in colour gradients and 2D colourmap) synchronously as their stellar population ages as indicated by D_{4000} and Hδ EW. This may be the general picture of how E+A galaxies evolve after the truncation of starburst possibly caused by the merger/interaction. It is a concern that our radial colour gradients do not show a tight correlation with Hδ EW, but the tendency of E+A galaxies with large positive slopes of radial colour gradient to show strong Hδ EWs. However, this may be affected by our cut-off of the inner region ($a/a_{60} < 0.35$) to avoid seeing effects when measuring radial colour gradients. Observation with high-resolution imaging might remove these effects, and produce a more accurate picture.

6 CONCLUSIONS

We have investigated morphologies, 2D colour property and radial colour gradients of 22 *true* E+A galaxies with $5.5\text{Å} < H\delta$ EW $< 8.5\text{Å}$ using the SDSS DR2 imaging data, in order to reveal evolution of E+A galaxies in terms of internal galaxy structures. We present this summary of our results:

- Concentration index, C_e, and our visual inspection of the SDSS images suggested that our E+A galaxies are predominantly bulge-dominated systems, and at least half of our E+A galaxies exhibit tidal features or disturbed morphologies.
- We found irregular 'Colour Morphologies' – asymmetrical and clumpy patterns – at the centre of $g-r$ and $r-i$ 2D colourmaps of the E+A galaxies.
- We found that a substantial number of E+A galaxies have positive slopes (bluer towards the centre) of radial $g-r$ and $r-i$ colour gradients.
- Kolomogorov-Smirnov two-sample tests showed that $g-r$ and $r-i$ colour gradient distributions of E+A galaxies are different from those of early-type galaxies with a more than 99.99% significance level.
- Our E+A sample showed tight correlation between radial colour gradients and colours, and between radial colour gradients and 4000Å break. We also found the tendency for E+A galaxies with large positive slopes of radial colour gradient to show strong Hδ EWs.
- The comparison between the GISSEL model (Bruzual & Charlot 2003) and E+A's observational quantities, Hδ EW, D_{4000} and $u-g$ colour, indicated that almost all our E+A galaxies are located along a single evolution track. Therefore, these results are interpreted as indicating E+A radial colour gradients evolve from positive into negative slopes, coherently with Hδ EW (8-5Å) within ∼300 Myr.

Our findings support the notion that E+A galaxies are post-starburst galaxies caused by merger/interaction, having undergone a centralized starburst. In addition, we presented a constraint on E+A's spatial evolution properties with a physical time scale. Detailed comparison with future theoretical simulations would advance our knowledge of the origin of E+A galaxies further.

ACKNOWLEDGMENTS

We thank Shin-ichi Ichikawa for useful discussions. We are grateful to Ani Thakar, Naoki Yasuda and Masafumi Yagi for gracious help with technical issues. We thank Simona Mei for useful suggestions for proofs. We thank Linux, XFree86, and other UNIX-related communities for the development of various useful software. This research has made use of the Plamo Linux.

REFERENCES

Abadi, M. G., Moore, B., & Bower, R. G. 1999, MNRAS, 308, 947

Abazajian, K., et al. 2003, AJ, 126, 2081

Abazajian, K., et al. 2004, AJ, 128, 502

Abraham, R. G., et al. 1996, ApJ, 471, 694

Bartholomew, L. J., Rose, J. A., & Gaba, A. E. 2001, AJ, 122, 2913

Barnes, J. E., & Hernquist L. 1992, ARA&A, 30, 705

Barger, A. J., Aragon-Salamanca, A., Ellis, R. S., Couch, W. J., Smail, I., & Sharples, R. M. 1996, MNRAS, 279, 1

Bruzual, A. G. 1983, ApJ, 273, 105

Bruzual, A. G., & Charlot, S. 2003, MNRAS, 344, 1000

Bekki, K. 1998, ApJ, 502, L133

Bekki, K., Shioya, Y., & Couch, W. J. 2001, ApJ, 547, L17

Belloni, P., Bruzual, A. G., Thimm, G. J., & Roser, H.-J. 1995, A&A, 297, 61

Blake, C., et al. 2004 MNRAS, 355, 713

Blanton, M. R., et al. 2003, AJ, 125, 2348

Broadhurst, T. J., Ellis, R. S., & Shanks, T. 1988, MNRAS, 235, 827

Caldwell, N., Rose, J. A., Sharples, R. M., Ellllis, R. S., & Bower, R. G. 1993, AJ, 106, 473

Caldwell, N., & Rose, J. A. 1997, AJ, 113, 492

Castander, F. J. et al. 2001, AJ, 121, 2331

Chang, T., van Gorkom, J. H., Zabludoff, A. I., Zaritsky, D., & Mihos, J. C. 2001, AJ, 121, 1965

Condon, J. J. 1992, ARA&A, 30, 575

Couch, W. J., & Shareples, R. M. 1987, MNRAS, 229, 423

Couch, W. J., Ellis, R. S., Sharples, R. M., & Smail, I. 1994, ApJ, 430, 121

Couch, W. J., Barger, A. J., Smail, I., Ellis, R. S., & Sharples, R. M. 1998, ApJ, 497, 188

Davis, R. L., Sadler, E. M., & Peletier R. F. 1993, MNRAS, 262, 650

de Vaucouleurs, G., de Vaucouleurs, A., Corwin, H., Buta, R., Paturel, G., & Fouqué, P. 1991, Third Reference Catalogue of Bright Galaxies (New York: Springer) (RC3)

Dressler, A., & Gunn, J. E. 1983, ApJ, 270, 7

Dressler, A., & Gunn, J. E. 1992, ApJS, 78, 1

Dressler, A., Oemler, A. J., Sparks, W. B., & Lucas, R. A. 1994, ApJ, 435, L23

Dressler, A., Smail, I., Poggianti, B. M., Butcher, H., Couch, W. J., Ellis, R. S., & Oemler, A. J. 1999, ApJS, 78, 1

Farouki, R., & Shapiro, S. L. 1980, ApJ, 241, 928

Fabricant, D. G., McClintock, J. E., & Bautz, M. W. 1991, ApJ, 381, 33

Fan, X. et al. 2003, AJ, 125, 1649

Fisher, D., Fabricant, D., Franx, M., & van Dokkum, P. 1998, ApJ, 498, 195

Franx, M. 1993, ApJ, 407, L5

Fujita, Y., & Nagashima, M. 1999, ApJ, 516, 619

Fujita, Y. 2004, PASJ, 56, 29

Fujita, Y., & Goto, T. 2004, PASJ, 56, 621

Fukugita, M., Ichikawa, T., Gunn, J. E., Doi, M., Shimasaku, K., & Schneider, D. P. 1996, AJ, 111, 1748

Goto, T., 2003, PhD Thesis, The University of Tokyo, astro-ph/0310196

Goto, T. et al. 2003a, PASJ, 55, 739

Goto, T., Okamura, S., Sekiguchi, M., et al. 2003b, PASJ, 55, 757

Goto, T. et al. 2003c, PASJ, 55, 771

Goto, T. et al. 2003d, PASJ, submitted

Goto, T., Yamauchi, C., Fujita, Y., Okamura, S., Sekiguchi, M., Smail, I., Bernardi, M., & Gomez, P. L. 2003e, MNRAS, 346, 601

Goto, T. 2004, A&A, 427, 125

Goto, T. 2005, MNRAS, 357, 937

Gunn, J. E., & Gott, J. R. I. 1972, ApJ, 176, 1

Gunn, J. E., et al. 1998, AJ, 116, 3040

Hogg, D. W., Schlegel, D. J., & Finkbeiner, D. P., & Gunn, J. E. 2001, AJ, 122, 2129

Hopkins, A. M., et al. 2003, ApJ, 599, 971

Kennicutt, R. C. 1992a, ApJS, 79, 255

Kennicutt, R. C. 1992b, ApJ, 388, 310

Kennicutt, R. C. 1998, ARA&A, 36 189

Kent, S. M. 1981, ApJ, 245, 805

Lavery, R. J. & Henry, J. P. 1986, ApJ, 304, L5

Lavery, R. J. & Henry, J. P. 1988, ApJ, 330, 596

Liu, C. T., & Kennicutt, R. C. 1995a, ApJS, 100, 325

Liu, C. T., & Kennicutt, R. C. 1995b, ApJ, 450, 547

Lupton, R. H., Gunn, J. E., Ivezic, Z., Knapp, G. R., Kent, S., & Yasuda, N. 2001, Astronomical Data Analysis Software and Systems X, ASP Conference Proceedings, 238, 269

MacLarn, I., Ellis, R. S., & Couch, W. J. 1988, MNRAS, 230, 249

Miller, N. A., & Owen, F. N. 2001, ApJ, 554, L25

Mihos, J. C., Richstone, D. O., & Bothun, G. D. 1992, ApJ, 400, 153

Mihos, J. C., & Heanquist, L. 1994, ApJ, 427, 112

Morris, S. J., Hutchings, J. B., Carlberg, R. G., Yee, H. K. C., Ellingson, E., Balogh, M. L., Abraham, R. G., & Smecker-Hane, T. A. 1998, ApJ, 507, 84

Newberry, M. V., Boroson, T. A., & Kirshner, R. P. 1990, ApJ, 350, 585

Nikolic, B., Cullen, H., & Alexander, P. 2004, MNRAS, 355, 874

Norton, S. A., Gebhardt, K., Zabludoff, A. I., & Zaritsky, D. 2001, ApJ, 557, 150

Oegerle, W. R., Hill, J. M., & Hoessel, J. G. 1991, ApJ, 381, L9

Oemler, A. J., Dressler, A., & Butcher, H. R. 1997, ApJ, 474, 561

Owen, F. N., Ledlow, M. J., Keel, W. C., & Morrison, G. E. 1999, AJ, 118, 633

Pier, J. R., Munn, J. A., Hindsley, R. B., Hennessy, G. S., Kent, S. M., Lupton, R. H., & Ivezic, Z. 2003, AJ, 125, 1559

Poggianti, B. M., & Wu, H. 2000, ApJ, 529, 157

Quilis, V., Moore, B., & Bower, R. 2000, Sci, 288, 1617

Quintero, A. D., et al. 2004, ApJ, 602, 190

Rose, J. A., Gaba, A. E., Caldwell, N., & Chaboyer, B. 2001, AJ, 121, 793

Salpeter, E. E. 1955, ApJ, 121, 161

Schlegel, D. J., Finkbeiner, D. P., & Davis, M. 1998, ApJ, 500, 525

Schweizer, F. 1982, ApJ, 252, 455

Schweizer, F. 1996, AJ, 111, 109

Sharples, R. M., Ellis, R. S., Couch, W. J., & Gray, P. M. 1985, MNRAS, 212, 687

Shimasaku, K. et al. 2001, AJ, 122, 1238

Smail, I., Dressler, A., Couch, W. J., Ellis, R. S., Oemler, A. J., Butcher, H., & Shaples, R. M. 1997, ApJS, 110, 213

Smail, I., Morrison, G., Gray, M. E., Owen, F. N., Ivison, R. J., Kneib, J.-P., & Ellis, R. S. 1999, ApJ, 525, 609

Smith, J. A., et al. 2002, AJ, 123, 2121

Spitzer, L. J., & Baade, W. 1951, ApJ, 113, 413

Stoughton, C., et al. 2002, AJ, 123, 485

Strateva, I., et al. 2001, AJ, 122, 1861

Strauss, M. A. et al. 2002, AJ, 124, 1810

Tanaka, M., Goto, T., Shimasaku, K., Okamura, S., Shimasaku, K., Brinkmann, J. 2004, ApJ, 128, 2677

Yamauchi, C., & Goto, T. 2004, MNRAS, 352, 815

Yamauchi, C., Ichikawa, S., Doi, M., Yasuda, N., Yagi M., Fukugita, M., Okamura, S., Nakamura, O., Sekiguchi, M., & Goto, T., AJ, submitted.

Yang, Y., Zabludoff, D., Zaritsky, D., Lauer, T., & Mihos, J. C. 2004, ApJ, 607, 258

York, D. G., et al. 2000, AJ, 120, 1579